From the $\gamma\gamma \to p\bar{p}$ reaction to the production of $p\bar{p}$ pairs in ultraperipheral ultrarelativistic heavy-ion collisions at the LHC

Mariola Kłusek-Gawenda,[1,*] Piotr Lebiedowicz,[1,†] Otto Nachtmann,[2,‡] and Antoni Szczurek[1,§]

[1]*Institute of Nuclear Physics Polish Academy of Sciences, Radzikowskiego 152, PL-31-342 Kraków, Poland*
[2]*Institut für Theoretische Physik, Universität Heidelberg, Philosophenweg 16, D-69120 Heidelberg, Germany*

In this paper we consider the production of proton-antiproton pairs in two-photon interactions in electron-positron and heavy-ion collisions. We try to understand the dependence of the total cross section on the photon-photon c.m. energy as well as corresponding angular distributions measured by the Belle Collaboration for the $\gamma\gamma \to p\bar{p}$ process. To understand the Belle data we include the proton-exchange, the $f_2(1270)$ and $f_2(1950)$ s-channel exchanges, as well as the hand-bag mechanism. The helicity amplitudes for the $\gamma\gamma \to f_2 \to p\bar{p}$ process are written explicitly based on a Lagrangian approach. The parameters of vertex form factors are adjusted to the Belle data. Having described the angular distributions for the $\gamma\gamma \to p\bar{p}$ process we present first predictions for the ultraperipheral, ultrarelativistic, heavy-ion reaction $^{208}Pb^{208}Pb \to {}^{208}Pb^{208}Pb\,p\bar{p}$. Both, the total cross section and several differential distributions for experimental cuts corresponding to the ALICE, ATLAS, CMS, and LHCb experiments are presented. We find the total cross section 100 μb for the ALICE cuts, 160 μb for the ATLAS cuts, 500 μb for the CMS cuts, and 104 μb taking into account the LHCb cuts. This opens a possibility to study the $\gamma\gamma \to p\bar{p}$ process at the LHC.

I. INTRODUCTION

The baryon pair production via $\gamma\gamma$ fusion was measured at electron-positron colliders by various experimental groups: CLEO [1] at CESR, VENUS [2] at TRISTAN, OPAL [3] and L3 [4] at LEP, and Belle [5] at KEKB. In the latter experiment the $\gamma\gamma \to p\bar{p}$ cross sections were extracted from the $e^+e^- \to e^+e^-p\bar{p}$ reaction for the $\gamma\gamma$ center-of-mass (c.m.) energy range of $2.025 < W_{\gamma\gamma} < 4$ GeV and in the c.m. angular range of $|\cos\theta| < 0.6$.

QCD predictions for $\gamma\gamma \to p\bar{p}$ were first calculated in [6,7] using the leading twist nucleon wave functions determined from QCD sum rules, see e.g. [8]. The calculated cross sections from the leading-twist QCD terms turned out to be about one order of magnitude smaller than the experimental data. To explain these experimental observations, various phenomenological approaches were suggested. For example, in the diquark model, which is a variant of the leading-twist approach, see e.g. [9] and references therein, the proton was considered to be a quark-diquark system and a diquark form factor was introduced. In the hand-bag approach, see e.g. [10], the $\gamma\gamma \to p\bar{p}$ amplitude was factorized into a hard $\gamma\gamma \to q\bar{q}$ subprocess

and form factors describing a soft $q\bar{q} \to p\bar{p}$ transition. The transition form factors could not be calculated from first principles in QCD and were, therefore, determined phenomenologically. The pQCD-inspired phenomenological models have more chances to describe the absolute size of the cross section for $W_{\gamma\gamma} > 2.5$ GeV, however, they contain a number of free parameters that are fitted to data. Moreover, most data were taken at energies which are rather low for the kinematic requirements of large s, $|t|$, $|u|$ in the hand-bag approach.

The low center-of-mass energy region of $\gamma\gamma \to p\bar{p}$ may be dominated by s-channel resonance contributions. One of the effective approaches used for this region is the Veneziano model [11]. While a reasonable $\sigma(W_{\gamma\gamma})$ dependence was obtained without adjustable parameters, the agreement of the model with the angular distributions was only qualitative.

In a recent calculation [12] only the proton exchange contribution was considered. But we think that this calculation has some problems as we shall discuss below in Sec. II A.

In our approach we wish to include all important theory ingredients in order to achieve a quantitative description of the Belle data. Then we present our predictions for the production of $p\bar{p}$ pairs in the ultraperipheral, ultrarelativistic, heavy-ion collisions at the LHC. To describe the dynamics of the $\gamma\gamma \to p\bar{p}$ process we take into account not only the nonresonant proton exchange contribution but also the s-channel tensor meson exchange contributions and the hand-bag mechanism. A measurement of the

*Mariola.Klusek@ifj.edu.pl
†Piotr.Lebiedowicz@ifj.edu.pl
‡O.Nachtmann@thphys.uni-heidelberg.de
§Also at Faculty of Mathematics and Natural Sciences, University of Rzeszów, Pigonia 1, PL-35-310 Rzeszów, Poland. Antoni.Szczurek@ifj.edu.pl
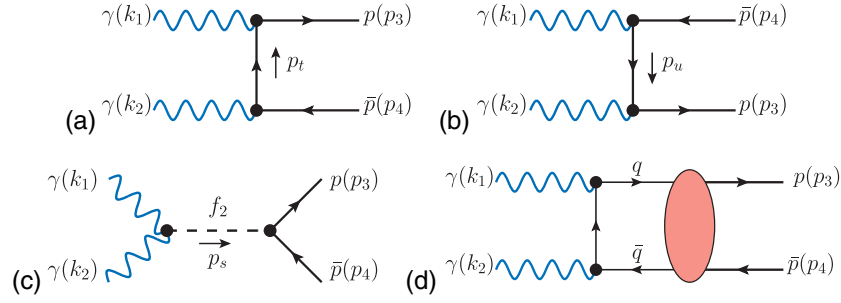
FIG. 1.   Diagrams for the production of $p\bar{p}$ in $\gamma\gamma$ collisions. We consider the t- and u-channel proton exchange [diagrams (a) and (b), respectively], the exchange of f_2 meson in the s-channel [diagram (c)], and the hand-bag mechanism [diagram (d) plus the one with the photon vertices interchanged]. Here f_2 stands generically for a $J^{PC} = 2^{++}$ meson.

$^{208}Pb^{208}Pb \rightarrow {}^{208}Pb^{208}Pb\,p\bar{p}$ reaction will provide further information on the two-photon interactions involved and, thus, will allow further tests of existing theoretical approaches.

II. THE $\gamma\gamma \rightarrow p\bar{p}$ REACTION

We consider the reaction (see Fig. 1)

$$\gamma(k_1, \epsilon_1) + \gamma(k_2, \epsilon_2) \rightarrow p(p_3, s_3) + \bar{p}(p_4, s_4),$$
$$s_3, s_4 \in \{1/2, -1/2\}, \qquad (2.1)$$

where the momenta, the polarization vectors of the photons, and the helicity indices for proton and antiproton are indicated in brackets. In the following we shall calculate the $\mathcal{T}$-matrix element for the reaction (2.1),

$$\langle p(p_3, s_3), \bar{p}(p_4, s_4)|\mathcal{T}|\gamma(k_1, \epsilon_1), \gamma(k_2, \epsilon_2)\rangle$$
$$= \mathcal{M}^{\mu\nu}(p_3, p_4; k_1, k_2)\epsilon_{1\mu}\epsilon_{2\nu}$$
$$\equiv \mathcal{M}_{\gamma\gamma \rightarrow p\bar{p}}, \qquad (2.2)$$

for nonresonant proton exchange, exchange of spin 2 mesons in the s-channel, and for the hand-bag mechanism. We note that gauge invariance requires

$$\mathcal{M}^{\mu\nu}(p_3, p_4; k_1, k_2)k_{1\mu} = 0,$$
$$\mathcal{M}^{\mu\nu}(p_3, p_4; k_1, k_2)k_{2\nu} = 0. \qquad (2.3)$$

Since the photons are bosons we must have

$$\mathcal{M}^{\mu\nu}(p_3, p_4; k_1, k_2) = \mathcal{M}^{\nu\mu}(p_3, p_4; k_2, k_1). \qquad (2.4)$$

The kinematical variables used in the present paper are (see Fig. 1)

$$s = (k_1 + k_2)^2 = (p_3 + p_4)^2 = W_{\gamma\gamma}^2,$$
$$t = (k_1 - p_3)^2 = (k_2 - p_4)^2,$$
$$u = (k_1 - p_4)^2 = (k_2 - p_3)^2,$$
$$s + t + u = 2m_p^2; \qquad (2.5)$$

$$p_s = k_1 + k_2 = p_3 + p_4,$$
$$p_t = k_2 - p_4 = p_3 - k_1,$$
$$p_u = k_1 - p_4 = p_3 - k_2; \qquad (2.6)$$

$$p_s^2 = s, \qquad p_t^2 = t, \qquad p_u^2 = u. \qquad (2.7)$$

We shall work in the c.m. frame of the reaction (2.1); see Fig. 18 in Appendix A. For the incoming photons we use the polarization vectors (A27) and the helicity spinors for the proton are as in (A2)–(A4) with $\theta \rightarrow \theta$, $\phi \rightarrow 0$. The helicity spinors for the antiproton are obtained from (A20) and (A10), (A11), with $\theta \rightarrow \pi - \theta$, $\phi \rightarrow \pi$.

There are 16 helicity amplitudes

$$\langle p(\mathbf{p_3}, s_3), \bar{p}(\mathbf{p_4}, s_4)|\mathcal{T}|\gamma(\mathbf{k_1}, m_1), \gamma(\mathbf{k_2}, m_2)\rangle$$
$$\equiv \langle 2s_3, 2s_4|\mathcal{T}|m_1, m_2\rangle. \qquad (2.8)$$

Here s_3, $s_4 \in \{1/2, -1/2\}$ and m_1, $m_2 \in \{1, -1\}$ are the helicity labels of proton, antiproton and the photons, respectively. We have also introduced a convenient short-hand notation for the amplitudes. Using rotational, parity, and charge-conjugation invariance one finds that only 6 of the 16 helicity amplitudes are independent which we denote by $\psi_1(s, t), \ldots, \psi_6(s, t)$; see (A39) and Table V of Appendix A.

The unpolarized differential cross section for the reaction (2.1) is given by

$$\frac{d\sigma}{d\cos\theta} = \frac{1}{32\pi s}\frac{|\mathbf{p_3}|}{|\mathbf{k_1}|}\frac{1}{4}\sum_{\text{spins}}|\mathcal{M}_{\gamma\gamma \rightarrow p\bar{p}}|^2, \qquad (2.9)$$

where s is the invariant mass squared of the $\gamma\gamma$ system, θ denotes the angle of the outgoing nucleon relative to the

beam direction in the c.m. frame, see Fig. 18 in Appendix A, and $\boldsymbol{k_1}$ and $\boldsymbol{p_3}$ are the c.m. 3-momenta of the initial photon and final nucleon, respectively; see (A26).

A. Nonresonant proton exchange contribution

The amplitude for the proton exchange mechanism [see the diagrams (a) and (b) in Fig. 1] is written as

$$\mathcal{M}_{\text{bare}}^{(p\,\text{exchange})} = (-i)\epsilon_{1\mu}\epsilon_{2\nu}\bar{u}(p_3)\Bigg(i\Gamma^{(\gamma pp)\mu}(p_3, p_t)$$

$$\times \frac{i(\not{p}_t + m_p)}{t - m_p^2 + i\epsilon} i\Gamma^{(\gamma pp)\nu}(p_t, -p_4)$$

$$+ i\Gamma^{(\gamma pp)\nu}(p_3, p_u)\frac{i(\not{p}_u + m_p)}{u - m_p^2 + i\epsilon}$$

$$\times i\Gamma^{(\gamma pp)\mu}(p_u, -p_4)\Bigg)v(p_4). \qquad (2.10)$$

Here we use the free proton propagator for the internal proton lines and the photon-proton vertex function as for on-shell protons respectively antiprotons. This photon-proton vertex function is, with $q = p' - p$, given by

$$i\Gamma_\mu^{(\gamma pp)}(p', p) = -ie\left[\gamma_\mu F_1(q^2) + \frac{i}{2m_p}\sigma_{\mu\nu}q^\nu F_2(q^2)\right];$$

$$(2.11)$$

see, e.g., (3.26) of [13]. In (2.11) $\sigma_{\mu\nu} = \frac{i}{2}[\gamma_\mu, \gamma_\nu]$, F_1 and F_2 are the Dirac and Pauli form factors of the proton, respectively. For real photons we have $F_1(0) = 1$ and $F_2(0) = \kappa_p = 1.7928$, where κ_p is the anomalous magnetic moment of the proton. The amplitude (2.10) satisfies the gauge-invariance relations (2.3) and the Bose-symmetry relation (2.4).

Of course, the virtual protons in the diagrams of Fig. 1(a) and 1(b) are off shell. Their propagators will, in general, not be the ones of free protons and the photon-proton vertex functions also will have an off-shell dependence. We take these off-shell dependences into account via multiplication of the amplitude (2.10) by an extra form factor. We adopt here the scheme used in previous works [14–17] and set

$$F(t, u, s) = \frac{[F(t)]^2 + [F(u)]^2}{1 + [\tilde{F}(s)]^2}, \qquad (2.12)$$

with the exponential parametrizations

$$F(t) = \exp\left(\frac{t - m_p^2}{\Lambda_p^2}\right),$$

$$F(u) = \exp\left(\frac{u - m_p^2}{\Lambda_p^2}\right),$$

$$\tilde{F}(s) = \exp\left(\frac{-(s - 4m_p^2)}{\Lambda_p^2}\right). \qquad (2.13)$$

The parameter Λ_p should be fitted to the experimental data. Note that the form factor $F(t)$ is normalized to unity for $t = m_p^2$.

Our complete result for the nonresonant proton exchange contribution reads, therefore,

$$\mathcal{M}^{(p\text{exchange})} = \mathcal{M}_{\text{bare}}^{(p\text{exchange})}F(t, u, s). \qquad (2.14)$$

The multiplication of the "bare" amplitude with a common form factor guarantees that the gauge-invariance relations (2.3) are satisfied for $\mathcal{M}^{(p\text{exchange})}$. Also the Bose-symmetry relation (2.4) is satisfied.[1] by (2.14) since $\mathcal{M}_{\text{bare}}^{(p\text{exchange})}$ satisfies (2.4) and the form factor $F(t, u, s)$ is symmetric under the exchange $t \leftrightarrow u$; see (2.10) and (2.12).

B. f_2 meson contributions

In this section we discuss the contributions from the s-channel exchange of $J^{PC} = 2^{++}$ mesons, generically denoted by f_2 in diagram (c) of Fig. 1. In the following we shall take into account the $f_2(1270)$ and $f_2(1950)$ resonances. That is, in the formulas f_2 stands for any of these resonances. In the final calculations their contributions are summed.

The amplitude for the $p\bar{p}$ production through the s-channel exchange of a tensor meson f_2 [the corresponding diagram is shown in Fig. 1(c)] is written as

$$\mathcal{M}^{(f_2\text{exchange})} = (-i)\bar{u}(p_3)i\Gamma^{(f_2p\bar{p})\alpha\beta}(p_3, p_4)v(p_4)i\Delta_{\alpha\beta,\kappa\lambda}^{(f_2)}(p_s)i\Gamma^{(f_2\gamma\gamma)\mu\nu\kappa\lambda}(k_1, k_2)\epsilon_{1\mu}\epsilon_{2\nu}. \qquad (2.15)$$

The $f_2\gamma\gamma$ vertex is given as

$$i\Gamma_{\mu\nu\kappa\lambda}^{(f_2\gamma\gamma)}(k_1, k_2) = i[2a_{f_2\gamma\gamma}F_a^{(f_2\gamma\gamma)}(p_s^2)\Gamma_{\mu\nu\kappa\lambda}^{(0)}(k_1, k_2) - b_{f_2\gamma\gamma}F_b^{(f_2\gamma\gamma)}(p_s^2)\Gamma_{\mu\nu\kappa\lambda}^{(2)}(k_1, k_2)], \qquad (2.16)$$

---

[1]The amplitude for $\gamma\gamma \to p\bar{p}$ considered in Eqs. (8)—(10) of [12] does not satisfy the Bose-symmetry relation (2.4). Therefore, this amplitude and the corresponding cross section, (16) and (20) of [12], cannot correspond to reality.

with two rank-four tensor functions,

$$\Gamma^{(0)}_{\mu\nu\kappa\lambda}(k_1, k_2) = [(k_1 \cdot k_2)g_{\mu\nu} - k_{2\mu}k_{1\nu}]\left[k_{1\kappa}k_{2\lambda} + k_{2\kappa}k_{1\lambda} - \frac{1}{2}(k_1 \cdot k_2)g_{\kappa\lambda}\right], \tag{2.17}$$

$$\Gamma^{(2)}_{\mu\nu\kappa\lambda}(k_1, k_2) = (k_1 \cdot k_2)(g_{\mu\kappa}g_{\nu\lambda} + g_{\mu\lambda}g_{\nu\kappa}) + g_{\mu\nu}(k_{1\kappa}k_{2\lambda} + k_{2\kappa}k_{1\lambda}) - k_{1\nu}k_{2\lambda}g_{\mu\kappa} - k_{1\nu}k_{2\kappa}g_{\mu\lambda} - k_{2\mu}k_{1\lambda}g_{\nu\kappa} - k_{2\mu}k_{1\kappa}g_{\nu\lambda}$$
$$- [(k_1 \cdot k_2)g_{\mu\nu} - k_{2\mu}k_{1\nu}]g_{\kappa\lambda}; \tag{2.18}$$

see (3.39) and (3.18)—(3.22) of [13]. In our case we have $k_1^2 = k_2^2 = 0$.

For the $f_2(1270)$ meson, the coupling constants $a_{f_2\gamma\gamma}$ and $b_{f_2\gamma\gamma}$ are estimated in Secs. 5.3 and 7.2 of [13]. In the case of the $f_2(1950)$ meson the numerical values of the a and b parameters will be obtained here from a fit to the Belle data [5]. In (2.16) we have introduced form factors $F^{(f_2\gamma\gamma)}_{a,b}(p_s^2)$ describing the s dependence of the $f_2\gamma\gamma$ coupling. These form factors will be particularly important for the diagram

Fig. 1(c) with $f_2(1270)$ exchange since in $p\bar{p}$ production this meson significantly contributes but only far off shell.

Let us now discuss in detail the $f_2 p\bar{p}$ vertex. From the l-S analysis, presented in Appendix B, we know that there are two independent couplings corresponding to $(l, S) = (1, 1)$ and $(3, 1)$. In accord with this we choose two coupling Lagrangians, (2.19) and (2.20) below, which correspond to two linearly independent combinations of the two (l, S) possibilities; see Appendix B. We set

$$\mathcal{L}'^{(1)}_{f_2pp}(x) = -\frac{g^{(1)}_{f_2pp}}{M_0}f_{2\kappa\lambda}(x)\frac{i}{2}\bar{\psi}_p(x) \times \left[\gamma^\kappa\overleftrightarrow{\partial}^\lambda + \gamma^\lambda\overleftrightarrow{\partial}^\kappa - \frac{1}{2}g^{\kappa\lambda}\gamma^\rho\overleftrightarrow{\partial}_\rho\right]\psi_p(x), \tag{2.19}$$

$$\mathcal{L}'^{(2)}_{f_2pp}(x) = \frac{g^{(2)}_{f_2pp}}{M_0^2}f_{2\kappa\lambda}(x)\bar{\psi}_p(x)\left[\overleftrightarrow{\partial}^\kappa\overleftrightarrow{\partial}^\lambda - \frac{1}{4}g^{\kappa\lambda}\overleftrightarrow{\partial}^\rho\overleftrightarrow{\partial}_\rho\right]\psi_p(x), \tag{2.20}$$

where $\psi_p(x)$ and $f_2(x)$ are the proton and f_2 meson field operators, respectively. The corresponding vertices, including form factors, are

$$i\Gamma^{(f_2p\bar{p})(1)}_{\kappa\lambda}(p_3, p_4) = -i\frac{g^{(1)}_{f_2pp}}{M_0}\left[\frac{1}{2}\gamma_\kappa(p_3 - p_4)_\lambda + \frac{1}{2}\gamma_\lambda(p_3 - p_4)_\kappa - \frac{1}{4}g_{\kappa\lambda}(\not{p}_3 - \not{p}_4)\right] \times F^{(f_2p\bar{p})(1)}[(p_3 + p_4)^2], \tag{2.21}$$

$$i\Gamma^{(f_2p\bar{p})(2)}_{\kappa\lambda}(p_3, p_4) = -i\frac{g^{(2)}_{f_2pp}}{M_0^2}\left[(p_3 - p_4)_\kappa(p_3 - p_4)_\lambda - \frac{1}{4}g_{\kappa\lambda}(p_3 - p_4)^2\right] \times F^{(f_2p\bar{p})(2)}[(p_3 + p_4)^2]. \tag{2.22}$$

Here $g^{(j)}_{f_2pp}$ ($j = 1, 2$) are dimensionless coupling constants and $M_0 \equiv 1$ GeV. The complete $f_2 p\bar{p}$ vertex function is given by

$$i\Gamma^{(f_2p\bar{p})}_{\kappa\lambda}(p_3, p_4) = \sum_{j=1,2}i\Gamma^{(f_2p\bar{p})(j)}_{\kappa\lambda}(p_3, p_4). \tag{2.23}$$

For the f_2 propagator we use the simple formula

$$i\Delta^{(f_2)}_{\alpha\beta,\kappa\lambda}(p_s) = iP^{(2)}_{\alpha\beta,\kappa\lambda}(p_s)\Delta^{(2)}(p_s^2) = i\left[\frac{1}{2}(\hat{g}_{\alpha\kappa}\hat{g}_{\beta\lambda} + \hat{g}_{\alpha\lambda}\hat{g}_{\beta\kappa}) - \frac{1}{3}\hat{g}_{\alpha\beta}\hat{g}_{\kappa\lambda}\right]\frac{1}{p_s^2 - m_{f_2}^2 + im_{f_2}\Gamma_{f_2}}, \tag{2.24}$$

where $\hat{g}_{\mu\nu} = -g_{\mu\nu} + p_{s\mu}p_{s\nu}/p_s^2$. Γ_{f_2} is the total decay width of the f_2 resonance and m_{f_2} its mass. For a more detailed analysis we should use a model for the f_2 propagator along the lines considered in [13]; see (3.6)—(3.8) and Appendix A of [13].

With the expressions from Appendix A we get the helicity amplitudes for the reaction $\gamma\gamma \to f_2 \to p\bar{p}$, using the notation of (A36) and $\varepsilon = (\varepsilon_{rs})$ as defined in (A16), as follows

$$\langle 2s_3, 2s_4|\mathcal{T}|+,+\rangle = \langle 2s_3, 2s_4|\mathcal{T}|-,-\rangle$$

$$= -\frac{1}{2}s^2\sqrt{s-4m_p^2}\Delta^{(2)}(s)a_{f_2\gamma\gamma}F_a^{(f_2\gamma\gamma)}(s) \times \left\{\frac{g_{f_2pp}^{(1)}}{M_0}F^{(f_2p\bar{p})(1)}(s)\left[-2m_p\left(\cos^2\theta-\frac{1}{3}\right)\delta_{s_3s_4}\right.\right.$$

$$\left.\left.-\sqrt{s}\sin\theta\cos\theta\varepsilon_{s_3s_4}\right] + \frac{g_{f_2pp}^{(2)}}{M_0^2}F^{(f_2p\bar{p})(2)}(s)(s-4m_p^2)\left(\cos^2\theta-\frac{1}{3}\right)\delta_{s_3s_4}\right\}, \tag{2.25}$$

$$\langle 2s_3, 2s_4|\mathcal{T}|\pm,\mp\rangle = -\frac{1}{2}s\sqrt{s-4m_p^2}\Delta^{(2)}(s)b_{f_2\gamma\gamma}F_b^{(f_2\gamma\gamma)}(s) \times \left\{\frac{g_{f_2pp}^{(1)}}{M_0}F^{(f_2p\bar{p})(1)}(s)[-2m_p\sin^2\theta\delta_{s_3s_4} + \sqrt{s}\sin\theta\cos\theta\varepsilon_{s_3s_4}\right.$$

$$\left.\pm\sqrt{s}\sin\theta\delta_{s_3,-s_4}] + \frac{g_{f_2pp}^{(2)}}{M_0^2}F^{(f_2p\bar{p})(2)}(s)(s-4m_p^2)\sin^2\theta\delta_{s_3s_4}\right\}. \tag{2.26}$$

Note the different s dependences in (2.25) and (2.26) that are due to the different dimensions of $a_{f_2\gamma\gamma}$ and $b_{f_2\gamma\gamma}$. Using different functional forms for the form factors F_a and F_b these s dependences could be adjusted to experimental data.

In the calculation we assume the same form for F_a and F_b

$$F_a^{(f_2\gamma\gamma)}(s) = F_b^{(f_2\gamma\gamma)}(s) = F^{(f_2\gamma\gamma)}(s). \tag{2.27}$$

A convenient ansatz for such a form factor is the exponential one (see (4.22) of [18])

$$F^{(f_2\gamma\gamma)}(s) = \exp\left(-\frac{(s-m_{f_2}^2)^2}{\Lambda_{f_2,exp}^4}\right) \tag{2.28}$$

with Λ_{f_2} a parameter of the order 1–2 GeV. Alternatively, we can use

$$F^{(f_2\gamma\gamma)}(s) = \frac{\Lambda_{f_2,pow}^4}{\Lambda_{f_2,pow}^4 + (s-m_{f_2}^2)^2}. \tag{2.29}$$

The form factors (2.28) and (2.29) are normalized to $F^{(f_2\gamma\gamma)}(m_{f_2}^2) = 1$. For the $f_2p\bar{p}$ form factors we assume

$$F^{(f_2p\bar{p})(1)}(s) = F^{(f_2p\bar{p})(2)}(s) = F^{(f_2\gamma\gamma)}(s). \tag{2.30}$$

The numerical values of the form factor parameters will be adjusted to the Belle experimental data.

C. Hand-bag approach

The hand-bag contribution to $\gamma\gamma \to B\bar{B}$ processes was described in detail in [10]. The hand-bag amplitude can be written in terms of the hard scattering kernel for $\gamma\gamma \to q\bar{q}$ and a soft matrix element describing the $q\bar{q} \to p\bar{p}$ transition. Their c.m. helicity amplitudes, which we denote by $\tilde{\mathcal{M}}$, are written in terms of the light-cone helicity amplitudes $\mathcal{A}$ (see Eq. (30) in [10]) as

$$\tilde{\mathcal{M}}_{s_3s_4,m_1m_2} = \mathcal{A}_{s_3s_4,m_1m_2} + \frac{m_p}{\sqrt{s}}[2s_3\mathcal{A}_{-s_3s_4,m_1m_2}$$

$$+ 2s_4\mathcal{A}_{s_3-s_4,m_1m_2}] + \mathcal{O}(m_p^2/s). \tag{2.31}$$

The light-cone helicity amplitudes, including terms suppressed only by $m_p/\sqrt{s}$, read [10]

$$\mathcal{A}_{s_3s_4,+-} = -(-1)^{s_3-s_4}\mathcal{A}_{-s_3-s_4,-+}$$

$$= 4\pi\alpha_{em}\frac{s}{\sqrt{tu}}\left\{\delta_{s_3,-s_4}\frac{t-u}{s}R_V(s) + 2s_3\delta_{s_3,-s_4}[R_A(s)\right.$$

$$\left.+ R_P(s)] - \frac{\sqrt{s}}{2m_p}\delta_{s_3s_4}R_P(s)\right\}. \tag{2.32}$$

The authors of [10] argue that the amplitudes with identical photon helicities will be nonzero only at next-to-leading order in α_s, in analogy to the photon helicity flip transitions in large-angle Compton scattering [19]. Note that for zero mass the light-cone helicity amplitudes (2.32) are identical with the helicity amplitudes (2.31), but not if the mass is finite. The $q\bar{q} \to p\bar{p}$ transition form factors $R_V(s)$, $R_A(s)$, and $R_P(s)$ were determined phenomenologically in [10]. In our calculation we neglect the term with $R_V(s)$ and assume $\frac{\sqrt{s}}{2m_p}|\frac{R_P(s)}{R_A(s)}| = 0.37$ (see formula (45) from [10]). In addition we take $R_A(s)$ and $R_P(s)$ as real and positive. We parametrize $R_A(s) = C_A/s$ (in parameter set A) with C_A a parameter of dimension GeV^2 or $R_A(s) = \tilde{C}_A/s^2$ (in parameter set B) with $\tilde{C}_A$ a parameter of dimension GeV^4 which we shall determine from a fit to the Belle data in Sec. IV C; see Table II. Note that the s-dependence of R_A with C_A is different (less steep) than in [10], where only the hand-bag contribution was fitted to rather old experimental data. In [10] different phase conventions compared to ours are used. Taking this into account we find

$$\langle 2s_3, 2s_4|\mathcal{T}|+,-\rangle_{hb} = 2s_4\tilde{\mathcal{M}}_{s_3s_4,+-},$$

$$\langle 2s_3, 2s_4|\mathcal{T}|-,+\rangle_{hb} = 2s_4\tilde{\mathcal{M}}_{s_3s_4,-+}; \tag{2.33}$$

see Appendix C.

The hand-bag helicity amplitudes (2.33) must be added coherently within our approach (see previous subsections).

At small momentum transfer $|t|$ or $|u|$ the hand-bag and proton-exchange mechanisms compete and it would be a double counting to include both of them simultaneously. We emphasize, however, that in regions of small $|t|$ or $|u|$ the hand-bag approach has to be taken with a grain of salt. To avoid in addition double counting (we include explicitly the proton-exchange mechanism) we suggest to multiply the hand-bag amplitudes by a purely phenomenological factor:

$$F_{\mathrm{corr}}(t, u) = \left(1 - \exp\left(\frac{t}{\Lambda_{hb}^2}\right)\right)\left(1 - \exp\left(\frac{u}{\Lambda_{hb}^2}\right)\right) \quad (2.34)$$

with an extra free parameter Λ_{hb}. Its role is to cut off the region of small $|t|$ and $|u|$ where the hand-bag approach does not apply. As a consequence it also reduces the hand-bag contribution to the cross section at low $\sqrt{s}$ in the whole angular range.

III. NUCLEAR REACTION

Now we will present theoretical formulas for the nuclear reaction

$$^{208}Pb + {}^{208}Pb \to {}^{208}Pb + {}^{208}Pb + p + \bar{p}. \quad (3.1)$$

We focus on the processes for ultraperipheral collisions (UPC) of heavy ions, see the diagram shown in Fig. 2. The nuclear cross section is calculated in the equivalent photon approximation (EPA) in the impact parameter space. This approach allows us to take into account the transverse distance between the colliding nuclei. The total (phase space integrated) cross section is expressed through the five-fold integral

$$\sigma_{AA \to AAp\bar{p}}(\sqrt{s_{AA}})$$
$$= \int \sigma_{\gamma\gamma \to p\bar{p}}(W_{\gamma\gamma}) N(\omega_1, \boldsymbol{b_1}) N(\omega_2, \boldsymbol{b_2}) S_{abs}^2(\boldsymbol{b})$$
$$\times \frac{W_{\gamma\gamma}}{2} dW_{\gamma\gamma} dY_{p\bar{p}} d\bar{b}_x d\bar{b}_y 2\pi b db. \quad (3.2)$$

Above, $b = |\boldsymbol{b}|$ is the impact parameter, i.e., the distance between colliding nuclei in the plane perpendicular to their direction of motion. $W_{\gamma\gamma} = \sqrt{4\omega_1\omega_2}$ is the invariant mass
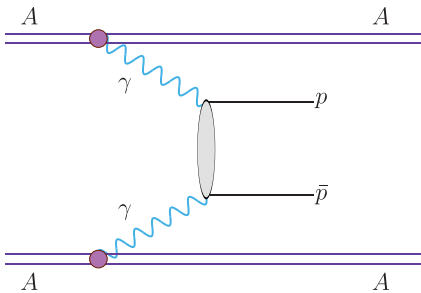
FIG. 2. Diagram representing proton-antiproton production in ultrarelativistic ultraperipheral collisions (UPC) of heavy ions.
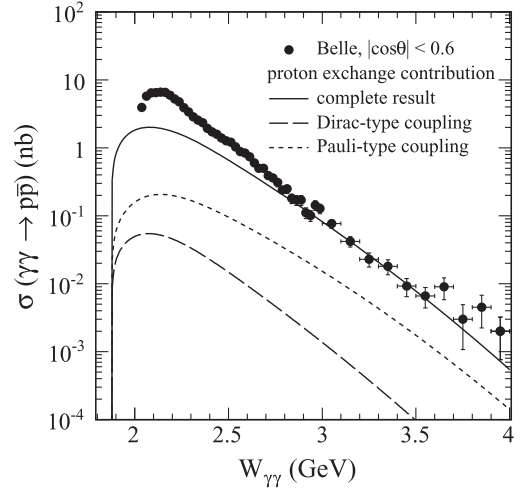
FIG. 3. The $\gamma\gamma \to p\bar{p}$ cross section as a function of photon-photon energy $W_{\gamma\gamma} \equiv \sqrt{s}$. We present the results for the nonresonant contribution (see Sec. II A) for $\Lambda_p = 1.1$ GeV in (2.13). The solid line represents the complete result with both Dirac- and Pauli-type couplings included in the amplitude. Other combinations of electromagnetic couplings in the γNN vertices are also shown: only Dirac couplings, and only Pauli couplings at the two vertices in Figs. 1(a) and 1(b). The Belle experimental data from [5] are shown for comparison.

of the $\gamma\gamma$ system and ω_i, $i = 1$, 2, is the energy of the photon which is emitted from the first or second nucleus, respectively. $Y_{p\bar{p}} = \frac{1}{2}(y_p + y_{\bar{p}})$ is the rapidity of the $p\bar{p}$ system. The quantities $\bar{b}_x = (b_{1x} + b_{2x})/2$, $\bar{b}_y = (b_{1y} + b_{2y})/2$ are given in terms of b_{ix}, b_{iy} which are the components of the $\boldsymbol{b_1}$ and $\boldsymbol{b_2}$ vectors which mark a point (distance from first and second nucleus) where photons collide and particles are produced. The diagram illustrating these quantities in the impact parameter space can be found in [20].
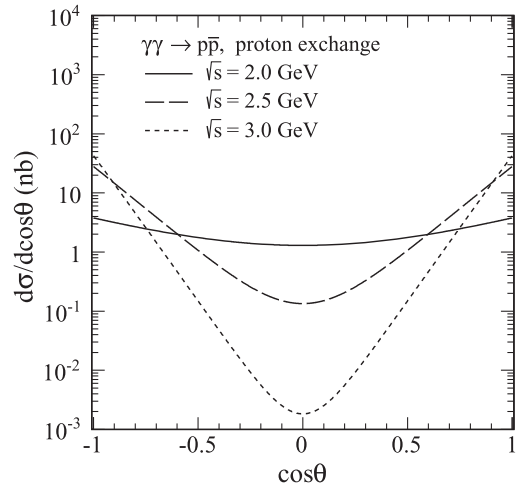
FIG. 4. The angular distributions for $\sqrt{s} = 2.0$, 2.5, and 3.0 GeV for the nonresonant proton-exchange mechanism.
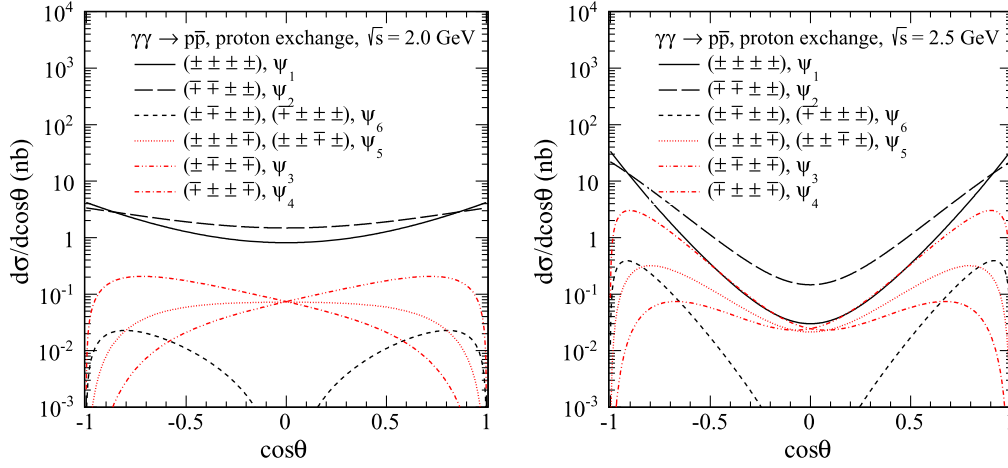
FIG. 5. The helicity components of $d\sigma/d\cos\theta$ as a function of $\cos\theta$ for the proton exchange mechanism for $\sqrt{s} = 2.0$ (the left panel) and 2.5 GeV (the right panel). Contributions of different helicities $(2s_3 2s_4 m_1 m_2)$ of the photons and baryons are shown.

In Ref. [20] the dependence of the photon flux $N(\omega_i, \mathbf{b}_i)$ on the charge form factors of the colliding nuclei was shown explicitly. In our calculations we use the so-called realistic form factor which is the Fourier transform of the charge distribution in the nucleus. A more detailed discussion of this issue is given in [20].

The presence of the absorption factor $S^2_{abs}(\mathbf{b})$ in (3.2) assures that we consider only peripheral collisions, when the nuclei do not undergo nuclear breakup. In the first approximation this geometrical factor can be expressed as

$$S^2_{abs}(\mathbf{b}) = \theta(|\mathbf{b}| - (R_A + R_B)) = \theta(|\mathbf{b}_1 - \mathbf{b}_2| - (R_A + R_B)),$$
(3.3)

where the sum of the radii of the two nuclei occurs.

In our present study we calculate also distributions in kinematical variables of each of the produced particles (for details on how it is handled see [21]). Then one can impose easily experimental cuts on (pseudo)rapidities and transverse momenta.

IV. RESULTS FOR THE $\gamma\gamma \to p\bar{p}$ REACTION

First we will show some features of the proton-exchange mechanism and the s-channel tensor meson exchanges. We

will show the dependence of the cross section on the photon-photon energy and the angular distributions of individual helicity components. Then we will confront the model results with the experimental data and adjust the model parameters.

A. Proton exchange mechanism

In Fig. 3 we show that the proton exchange mechanism alone cannot describe the energy-dependence of the cross sections measured by Belle [5]. We show results for the Dirac- or Pauli-type couplings separately and when both couplings in the γNN vertices are taken into account. We can see that the complete result indicates a large interference effect of Dirac and Pauli terms in the amplitudes. Clearly, the proton exchange contribution is not sufficient to describe the Belle data.

In Fig. 4 we show the unpolarized differential cross section $d\sigma/d\cos\theta$ for three different $\gamma\gamma$ c.m. energies. As one gets closer to $\sqrt{s} = 2m_p$, the threshold energy, the angular distributions become flatter and flatter.

In Fig. 5 we present the helicity dependence of the differential cross section. We label the results for different helicity terms as $(2s_3 2s_4 m_1 m_2)$ for $\langle 2s_3, 2s_4 | \mathcal{T} | m_1, m_2 \rangle$ as defined in (A36). One can see the dominance of the

TABLE I. A list of resonances that may contribute to the $\gamma\gamma \to p\bar{p}$ reaction. Here we listed also the subthreshold $f_2(1270)$ resonance. The meson masses, their total widths Γ, and branching fractions are taken from PDG [24].

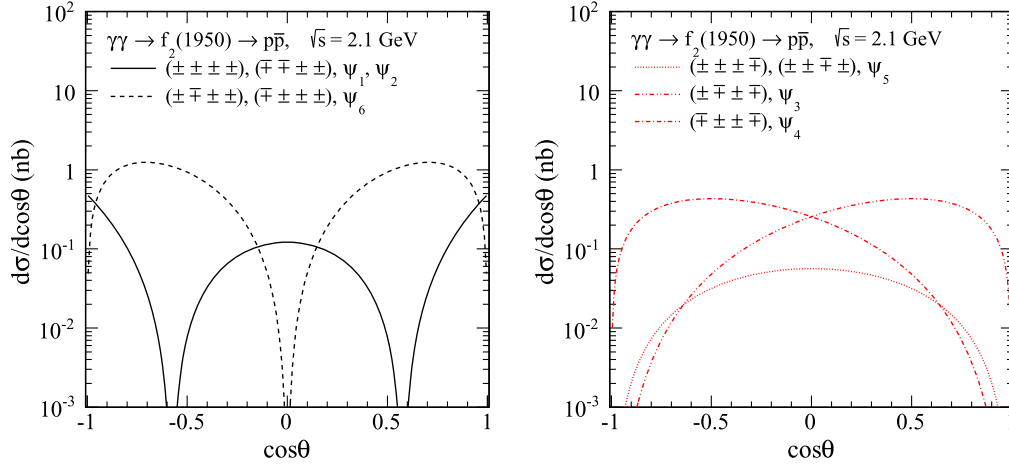| Meson	m (MeV)	Γ (MeV)	$\Gamma_{p\bar{p}}/\Gamma$	$\Gamma_{\gamma\gamma}/\Gamma$
$f_2(1270)$	1275.5 ± 0.8	$186.7^{+2.2}_{-2.5}$		$(1.42 \pm 0.24) \times 10^{-5}$
$f_2(1950)$	1944 ± 12	472 ± 18	seen	seen
$\eta_c(1S)$	2983 ± 0.5	31.8 ± 0.8	$(1.50 \pm 0.16) \times 10^{-3}$	$(1.59 \pm 0.13) \times 10^{-4}$
$\chi_{c0}(1P)$	3414.75 ± 0.31	10.5 ± 0.6	$(2.25 \pm 0.09) \times 10^{-4}$	$(2.23 \pm 0.13) \times 10^{-4}$
$\chi_{c2}(1P)$	3556.20 ± 0.09	1.93 ± 0.11	$(7.5 \pm 0.4) \times 10^{-5}$	$(2.74 \pm 0.14) \times 10^{-4}$
$\eta_c(2S)$	3639.2 ± 1.2	$11.3^{+3.2}_{-2.9}$	$< 2 \times 10^{-3}$	$(1.9 \pm 1.3) \times 10^{-4}$

FIG. 6. The helicity components of the differential cross sections $d\sigma/d\cos\theta$ for the $\gamma\gamma \to f_2(1950) \to p\bar{p}$ reaction for $\sqrt{s} = 2.1$ GeV. Here, the coupling constants are fixed arbitrarily, for $j = 1, 2$: $a_{f_2\gamma\gamma}g_{f_2pp}^{(j)} = \frac{e^2}{4\pi}1$ GeV^{-3} (the left panel) and $b_{f_2\gamma\gamma}g_{f_2pp}^{(j)} = \frac{e^2}{4\pi}1$ GeV^{-1} (the right panel). The calculations have been done for $\Lambda_{f_2,pow} = 1.15$ GeV in (2.29).
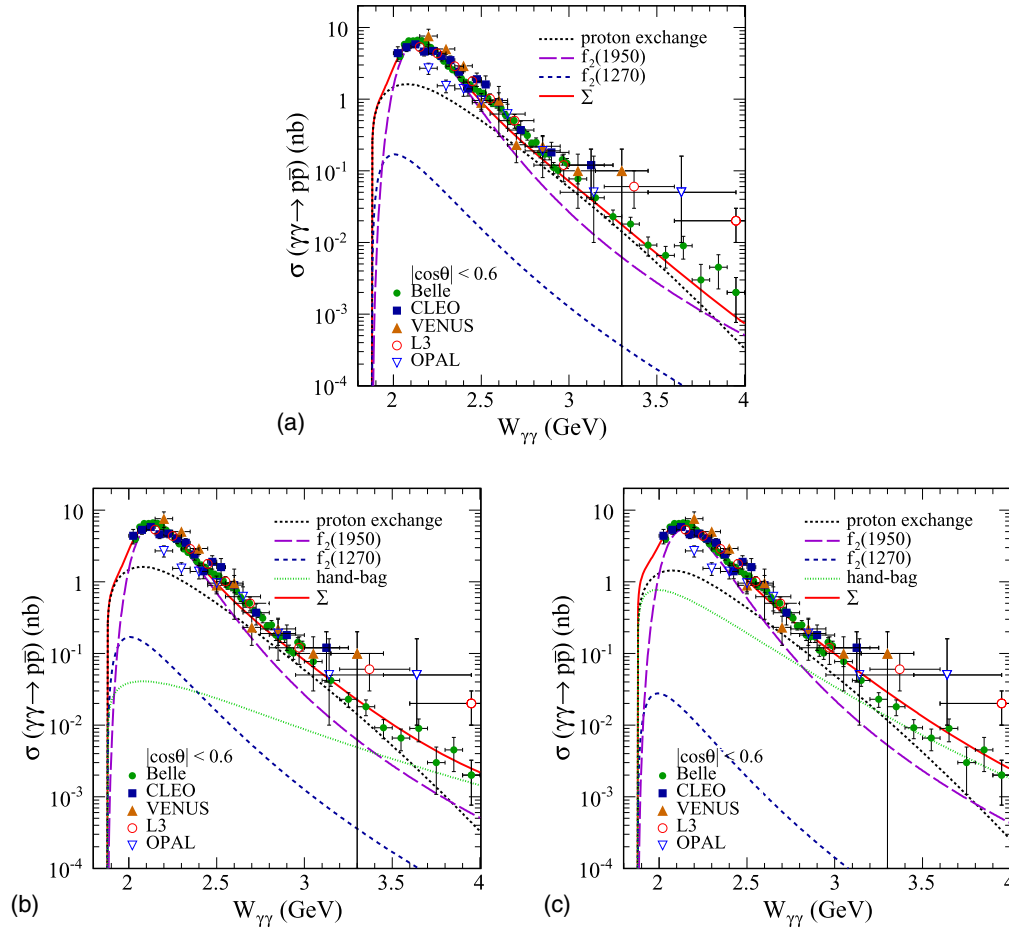

FIG. 7. Energy dependence of the total cross section for $\gamma\gamma \to p\bar{p}$ for $|\cos\theta| < 0.6$. The experimental data are from the CLEO [1], VENUS [2], OPAL [3], L3 [4], and Belle [5] experiments. In the panel (a) we show the results for the tensor meson exchanges and the proton-exchange contributions, and their coherent sum (see the red solid line). In the panels (b) and (c) we show the results including, in addition, the hand-bag contribution. In the panels (a) and (b) we used the parameter set A while in the panel (c) we used the parameter set B; see Table II.

TABLE II. Model parameters and their numerical values used. The second column indicates the equation numbers where the parameter is defined.

parameter for nonresonant $p\bar{p}$	equation	value (set A)	value (set B)
κ_p	(2.11) et subeqution	1.7928	1.7928
Λ_p	(2.12), (2.13)	1.08 GeV	1.07 GeV
$f_2(1270)$			
$a_{f_2\gamma\gamma}$	(2.16); (3.40) of [13]	$\frac{e^2}{4\pi}$1.45 GeV^{-3}	$\frac{e^2}{4\pi}$1.45 GeV^{-3}
$b_{f_2\gamma\gamma}$	(2.16); (3.40) of [13]	$\frac{e^2}{4\pi}$2.49 GeV^{-1}	$\frac{e^2}{4\pi}$2.49 GeV^{-1}
M_0	(2.19) et subeqution	1 GeV	1 GeV
$g_{f_2pp}^{(1)}$	(2.19), (2.21)	11.04	11.04
$g_{f_2pp}^{(2)}$	(2.20), (2.22)	0	0
$\Lambda_{f_2,pow}$	(2.29)	1.15 GeV	1 GeV
$f_2(1950)$			
$a_{f_2\gamma\gamma}g_{f_2pp}^{(2)}$	(2.16), (2.20), (2.22)	$\frac{e^2}{4\pi}$13.05 GeV^{-3}	$\frac{e^2}{4\pi}$12 GeV^{-3}
$b_{f_2\gamma\gamma}$	(2.16)	0	0
$g_{f_2pp}^{(1)}$	(2.19), (2.21)	0	0
$\Lambda_{f_2,pow}$	(2.29)	1.15 GeV	1.15 GeV
hand-bag contribution			
C_A	$R_A(s) = C_A/s$	0.14 GeV^2	
$\tilde{C}_A$	$R_A(s) = \tilde{C}_A/s^2$		2.5 GeV^4
Λ_{hb}	(2.34)	0.85 GeV	0.85 GeV

$(\pm \pm \pm \pm)$ and $(\mp \mp \pm \pm)$ contributions over the $(2s_3 2s_4 \pm \mp)$ ones (see the red lines). In terms of the ψ_j $(j = 1, ..., 6)$ from (A39) and Table V of Appendix A we find dominance of the amplitudes ψ_1 and ψ_2. Furthermore we see that the contributions of the amplitudes ψ_3, ψ_4, ψ_5, and ψ_6 are suppressed in the forward and backward directions, $\cos\theta = \pm 1$. This is clear from angular momentum conservation. For ψ_3, ψ_4, and ψ_5, the state of the two photons has $J_z = \pm 2$. This cannot be reached by proton-antiproton produced in the forward or backward direction where we only get $J_z = 0$ or ± 1. For ψ_6 the two-photon state has $J_z = 0$ and the two-baryon state in forward and backward direction has $J_z = +1$ and -1, respectively. We have again a mismatch. The contributions of four helicity states $(+ - + +)$, $(- + - -)$, $(- + + +)$, $(+ - - -)$ vanish when only the Dirac-type coupling in the γNN vertices is included. That is, the amplitude ψ_6 vanishes in this case.

B. f_2 meson contributions

The Belle experimental angular distributions [5], at least at low energies, cannot be described solely with the proton-exchange mechanism discussed in Sec. II A. It seems that a mechanism is missing. A resonant s-channel contribution is a reasonable option for a second mechanism (see also [16] for the $\gamma\gamma \to \pi\pi$ reactions).

In Table I we have listed resonances that decay into $\gamma\gamma$ and $p\bar{p}$ and which, therefore, may contribute to the reaction (2.1). In principle, also subthreshold resonances, such as

$f_2(1270)$, may play some, even an important, role. It is worth to mention that our knowledge about the $f_2(1950)$ resonance comes from the BES [22] and the CLEO [23] analyses for $\psi(2S) \to \gamma p\bar{p}$ radiative decays. In [23] the authors include also the $f_2(2150) \to p\bar{p}$ contribution in order to describe the $M_{p\bar{p}}$ and $M_{p\gamma}$ invariant mass distributions. For $\psi(2S) \to \gamma p\bar{p}$ a stringent upper limit for the threshold resonance $\mathcal{B}(\psi(2S) \to \gamma R_{thr}) \times \mathcal{B}(R_{thr} \to p\bar{p}) < 1.6 \times 10^{-5}$ at 90% confidence level was found [23].

In our paper we consider only the f_2 meson exchanges in the s-channel. In general also the $c\bar{c}$ mesons (e.g., $\eta_c(1S)$, $\chi_{c0}(1P)$) may contribute to the reaction (2.1). The charmonium states have rather small total widths (see Table I) thus they will appear in the invariant mass distribution as rather narrow peaks; see [25] for the $\gamma\gamma \to \gamma\gamma$ reaction. Even interference effects with other mechanisms may be important in this context. This goes, however, beyond the scope of the present paper and will be studied elsewhere.

Now we will discuss the helicity structure of $\gamma\gamma \to p\bar{p}$ from the contribution of the s-channel (below-threshold or above-threshold) f_2 resonances in our Lagrangian approach; see Sec. II B.

In Fig. 6 we show the contributions of different helicities for the two $\gamma\gamma \to f_2$ couplings in (2.16), $a_{f_2\gamma\gamma}$ (left panel), and $b_{f_2\gamma\gamma}$ (right panel). There are five independent helicity contributions since here the contributions of the amplitudes ψ_1 and ψ_2 turn out to be the same; see (2.25), (A39), and Table V of Appendix A. Only the distributions that are
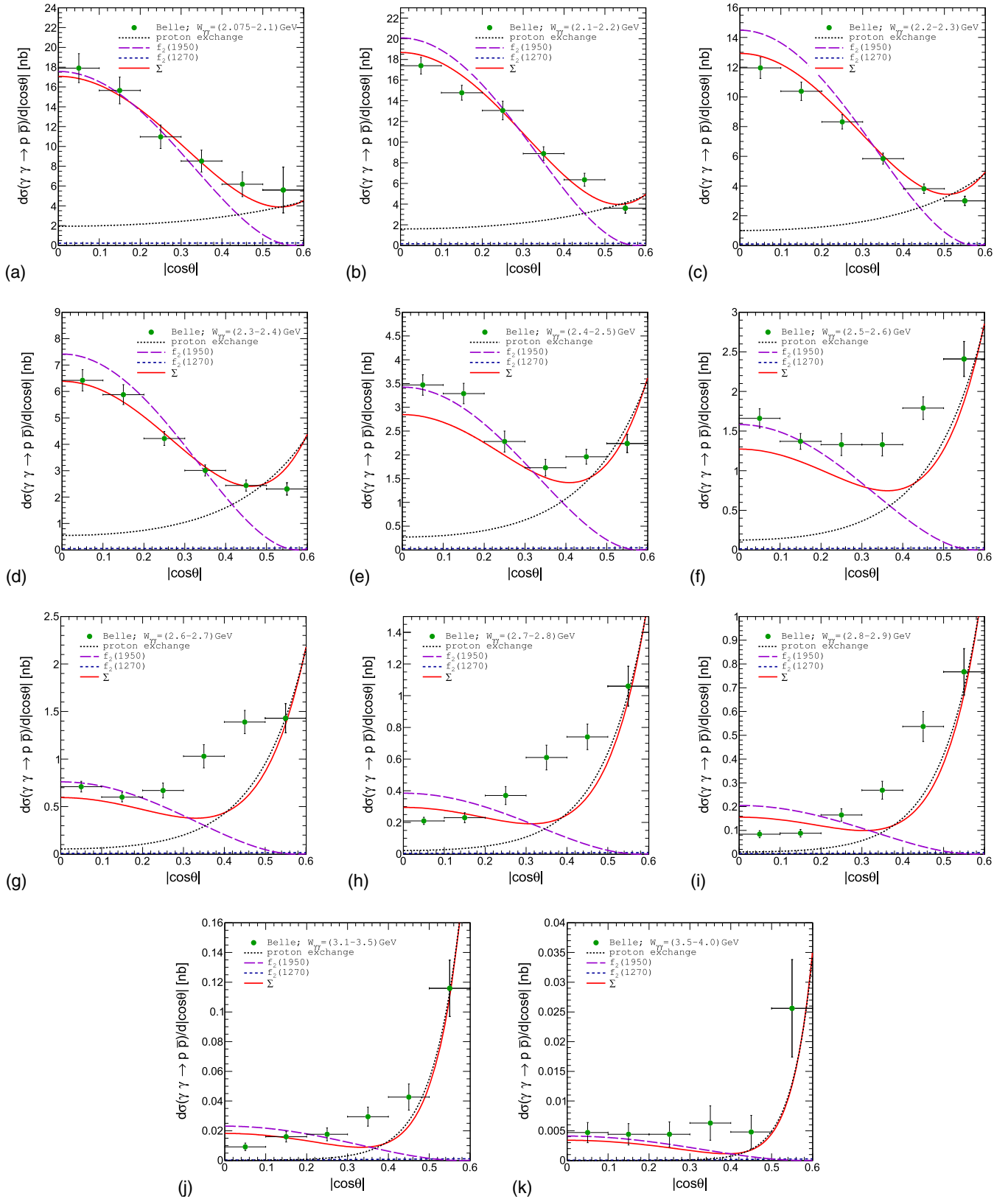
FIG. 8.   Differential cross sections for the $\gamma\gamma \to p\bar{p}$ reaction as a function of $|\cos\theta|$ for different $W_{\gamma\gamma}$ ranges. For the Belle data [5] both statistical and systematic uncertainties are included. Calculations were done with $\Lambda_{f_2,pow} = 1.15$ GeV in (2.29), and $\Lambda_p = 1.08$ GeV in (2.13). The hand-bag model contribution is not included here. Here we used the parameter set A from Table II.
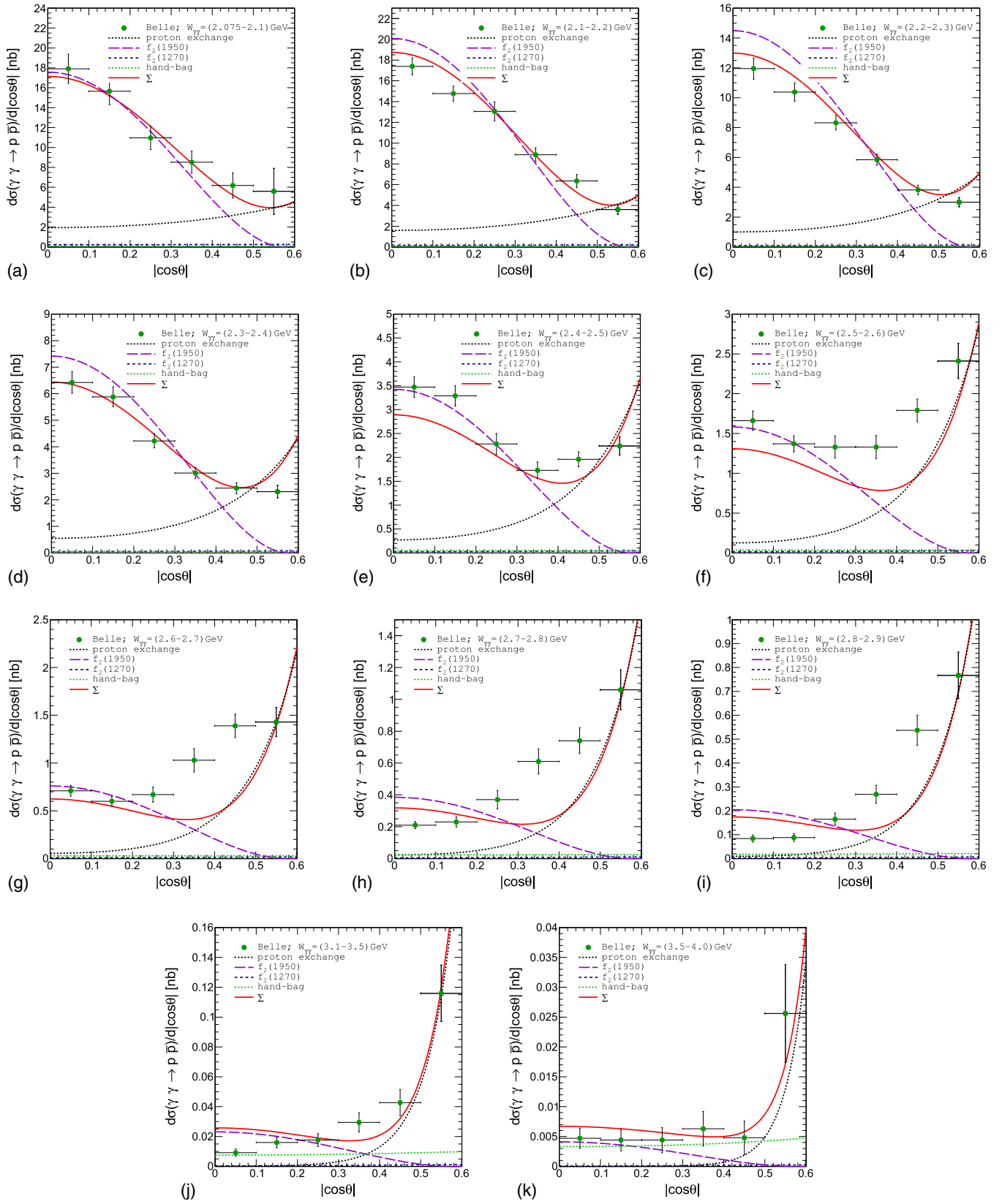
FIG. 9. The same as in Fig. 8 but here the hand-bag contribution is included. The green dotted line shows the contribution of the hand-bag mechanism. Here we used the parameter set A from Table II.
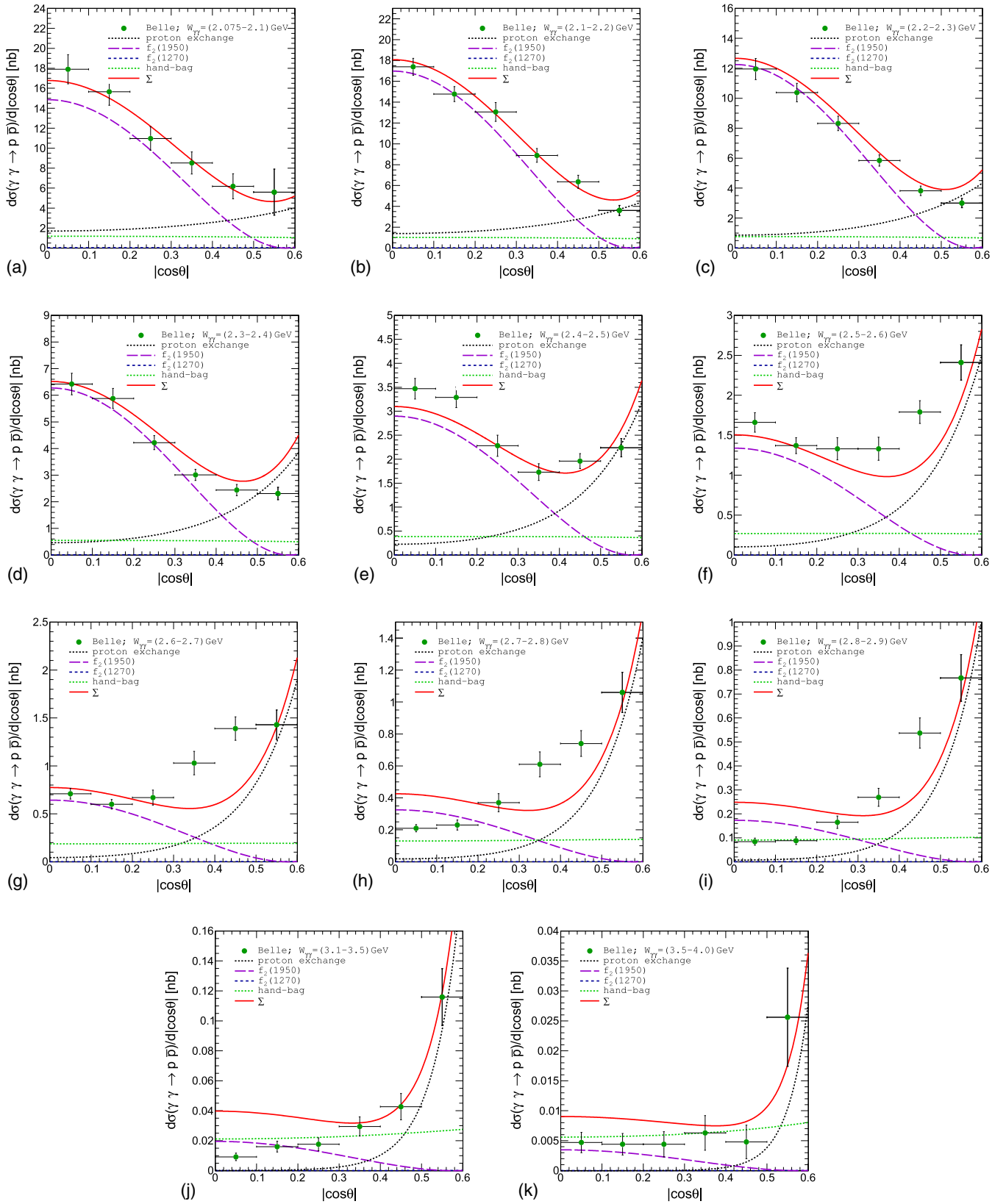
FIG. 10.   The same as in Fig. 9 but here we used the parameter set B from Table II.
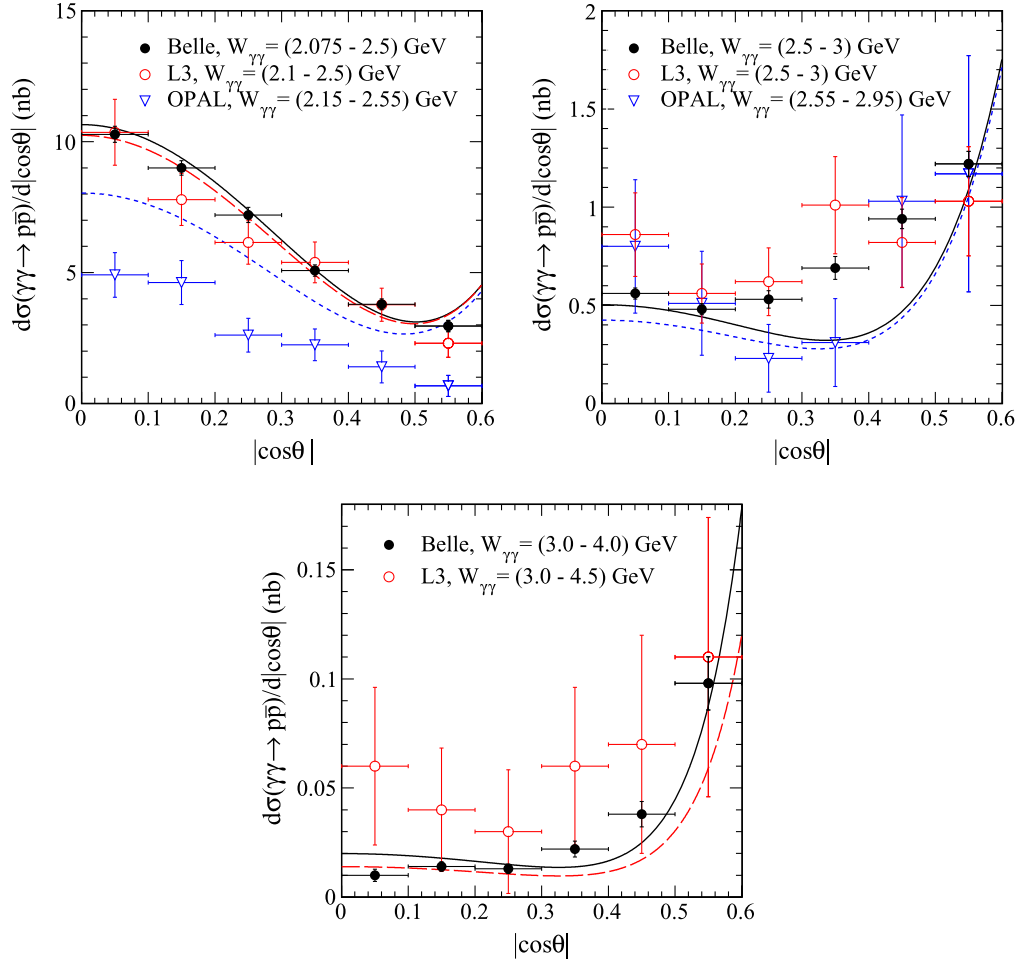
FIG. 11. Differential cross sections for the $\gamma\gamma \to p\bar{p}$ reaction as a function of $|\cos\theta|$ for different $W_{\gamma\gamma}$ ranges. We compare our total model results (including the hand-bag contribution) with the Belle data [5], the L3 data [4], and the OPAL data [3]; see the black solid line, the red long-dashed line, and the blue short-dashed line, respectively. Here we used the parameter set A from Table II.

proportional to $(\cos^2\theta - 1/3)^2$, see (2.25) and (2.26), (this corresponds to the solid line in the left panel) are favored by the Belle experimental data; see Figs. 8 and 9 below. Here the cutoff parameter of form factors ($\Lambda_{f_2,pow}$) and the products of coupling constants ($a_{f_2\gamma\gamma}g^{(j)}_{f_2pp}$ and $b_{f_2\gamma\gamma}g^{(j)}_{f_2pp}$) are fixed arbitrarily.

C. Comparison with the Belle data

Here we wish to demonstrate that it is possible to describe the Belle data taking into account the t- and u-channel proton exchanges, the s-channel tensor meson exchanges, and the hand-bag mechanism discussed in Sec. II. In the following we shall take in our calculation a coherent sum of all the above amplitudes.

In Fig. 7 we show the energy dependence of the cross section for the $\gamma\gamma \to p\bar{p}$ reaction. In the panel (a) we present results for the proton exchange and the $f_2(1270)$ and $f_2(1950)$ s-channel exchanges together with the experimental data of the CLEO [1], VENUS [2], OPAL

[3], L3 [4], and Belle [5] experiments. An agreement between the Belle experimental data [5] and the earlier measurements [1,2,4] with the exception of the OPAL experiment [3] in the low mass region $W_{\gamma\gamma} = M_{p\bar{p}} < 3$ GeV can be observed (within the quoted uncertainties); see also Fig. 11 below. For the $f_2(1270)$ contribution the coupling constants $a_{f_2\gamma\gamma}$ and $b_{f_2\gamma\gamma}$ are relatively well known and taken from [13]. We take into account only one $f_2(1270)p\bar{p}$ coupling ($g^{(1)}_{f_2(1270)pp} = 11.04$) and neglect the term with $g^{(2)}_{f_2(1270)pp}$. For the $f_2(1950)$ contribution we take only the term with $a_{f_2(1950)\gamma\gamma}g^{(2)}_{f_2(1950)p\bar{p}} = \frac{e^2}{4\pi}13.05$ GeV^{-3}. In the vertices for the meson exchange contributions we assume the same type of the form factors (2.29) and $\Lambda_{f_2,pow} = 1.15$ GeV; see Eqs. (2.27) and (2.30). We take $\Lambda_p = 1.08$ GeV for the proton-exchange contribution; see (2.13). One can observe the dominance of the $f_2(1950)$ resonance term at low energies. We slightly underestimate the Belle data from $\sqrt{s} = 2.4$ to 2.9 GeV.

The panels (b) and (c) show results including also the hand-bag contribution. The hand-bag contribution is important at $W_{\gamma\gamma} > 3$ GeV. To illustrate uncertainties of our model we take in the calculation two sets of parameters. For the convenience of the reader we collect in Table II the parameters of our model and their numerical values used here and in the following.

In Figs. 8 and 9, we show our fits to the Belle angular distributions[2] Here we use the same parametrization as in Fig. 7(a) (see set A of Table II). In Fig. 8 we present results for the $f_2(1270)$, $f_2(1950)$ and proton-exchange contributions separately, as well as their coherent sum. At large angles, $\cos\theta \approx 0$, the inclusion of the $f_2(1270)$ contribution lowers the cross section compared to the case when only the $f_2(1950)$ and proton-exchange are taken into account. In Fig. 9 we show results including the hand-bag contribution. The C_A parameter obtained from the fit is $C_A = 0.14$ GeV^2. In Fig. 10 we use, as in Fig. 7(c), the parameter set B of Table II. The $\tilde{C}_A$ parameter obtained from the fit is $\tilde{C}_A = 2.5$ GeV^4. In Ref. [10] $\tilde{C}_A$ was estimated to be in the range $4.9 \div 8.0$ GeV^4 which is the same order of magnitude as we find.

Experimentally the angular distributions were averaged over rather large intervals of (sub)process energies. For a better comparison with the experimental data we use the formula, with $z \equiv \cos\theta$,

$$\left\langle \frac{d\sigma}{dz}(W_{\gamma\gamma}) \right\rangle_{\Delta W_{\gamma\gamma}} = \frac{1}{\Delta W_{\gamma\gamma}} \int_{W_{\gamma\gamma}-\frac{\Delta W_{\gamma\gamma}}{2}}^{W_{\gamma\gamma}+\frac{\Delta W_{\gamma\gamma}}{2}} \frac{d\sigma}{dz}(W_{\gamma\gamma}) dW_{\gamma\gamma}, \quad (4.1)$$

instead of $\frac{d\sigma}{dz}(W_{\gamma\gamma} = \frac{W_{\gamma\gamma,min}+W_{\gamma\gamma,max}}{2})$.

In Fig. 11 we compare the Belle data [5] and the earlier OPAL and L3 data [3,4] with our model results. Due to the large error bars of the OPAL and L3 data only the comparison of the model results with the Belle data gives significant information.

Heaving shown that the results of our approach, including three mechanisms, describe the Belle experimental data reasonably well we shall present our predictions for the nuclear reaction (3.1) in the next section.

V. PREDICTIONS FOR THE NUCLEAR ULTRAPERIPHERAL COLLISIONS

Having described the Belle angular distributions we go to the predictions for the nuclear collisions. In this section we show the integrated cross sections and several differential distributions for the nuclear process (3.1) calculated as described in Sec. III including three mechanisms discussed in Secs. II and IV. In the calculations below we used the parameter set A from Table II.

---

[2]The cross section $d\sigma/d|z|$, $z = \cos\theta$, was calculated for the Belle angular range of $-0.6 < z < 0.6$, but plotted for $0 < z < 0.6$ after multiplication by a factor 2.
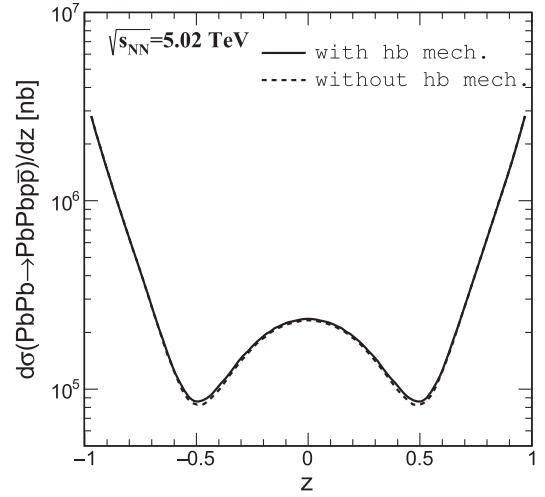

FIG. 12. The distribution in $z = \cos\theta$, integrating over $2m_p < W_{\gamma\gamma} < 4$ GeV, for the $PbPb \to PbPbp\bar{p}$ reaction at the $PbPb$ collision energy $\sqrt{s_{NN}} = 5.02$ TeV.

In Fig. 12 we present the angular distribution $d\sigma/dz$ ($z = \cos\theta$ in the $\gamma\gamma$ c.m. system) at the $PbPb$ collision energy $\sqrt{s_{NN}} = 5.02$ TeV. Here we show the nuclear results when the hand-bag mechanism is included (solid line) and excluded (dotted line). One can conclude that the hand-bag contribution does not play an important role in the $p\bar{p}$ angular distribution. We wish to emphasize that the enhancements at $z = \pm 1$ are the consequence of our model presented in Sec. II. One can better visualize this behavior with the help of the two dimensional distribution $d^2\sigma/dzdW_{\gamma\gamma}$. From Fig. 13 we clearly see that the result for the nuclear reaction corresponds to that for elementary $\gamma\gamma \to p\bar{p}$ reaction discussed in the previous section. The $f_2(1950)$ contribution dominates at smaller $W_{\gamma\gamma}$ and at $z \approx 0$ and $z \approx \pm 1$. This coincides with the result which was presented in Fig. 6 (left panel, solid line). In contrast to the
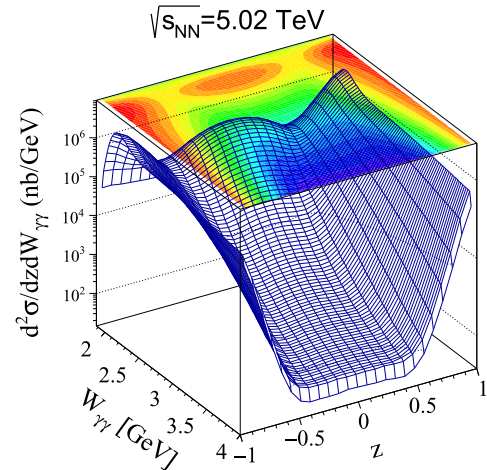

FIG. 13. Distribution in $(z, W_{\gamma\gamma})$ for the $PbPb \to PbPbp\bar{p}$ reaction (3.1) at the LHC energy $\sqrt{s_{NN}} = 5.02$ TeV.
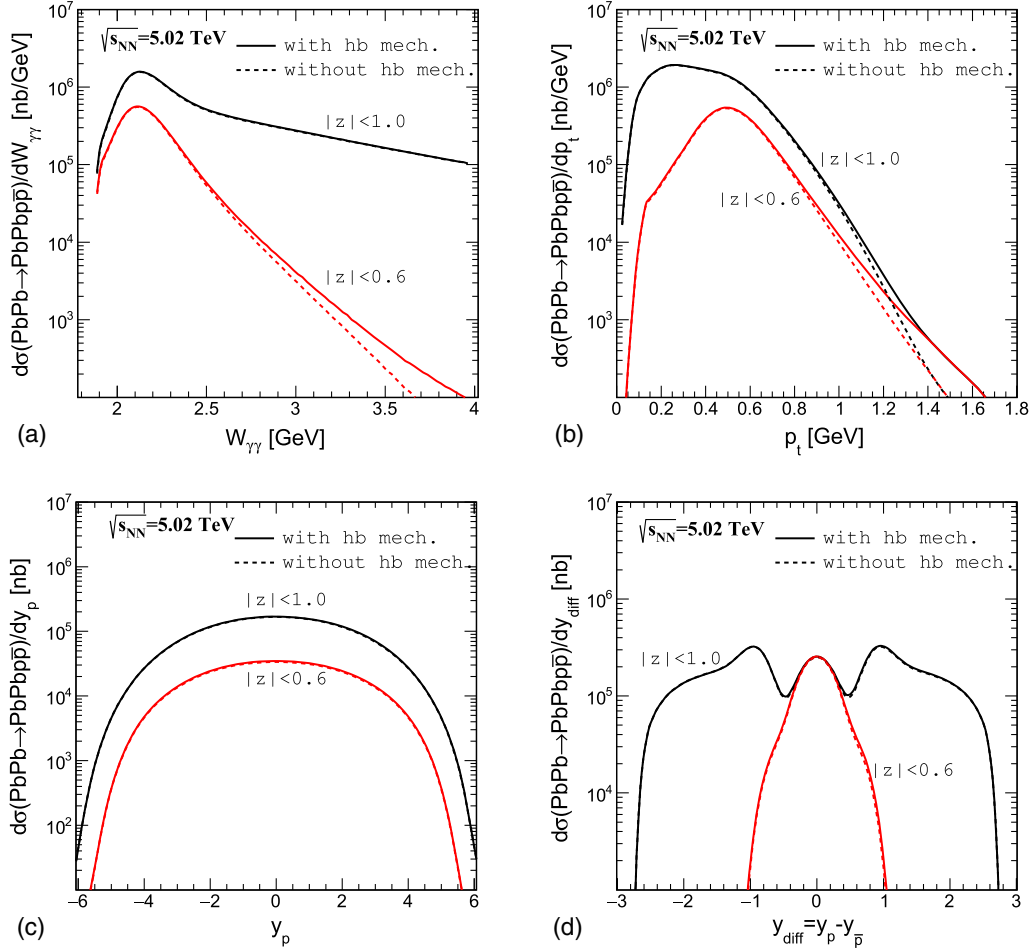
FIG. 14. The differential nuclear cross sections for the $PbPb \to PbPbp\bar{p}$ reaction (3.1) at $\sqrt{s_{NN}} = 5.02$ TeV. Results for the full range of z (the black lines) and for $|z| < 0.6$ (the red lines) are presented. In panels (b)—(d) we integrate for $2m_p \leq W_{\gamma\gamma} < 4$ GeV. No other cuts have been imposed here.

resonant contribution, the proton-exchange one is concentrated mostly at larger invariant masses and around $z = \pm 1$.

In Fig. 14 we present the nuclear differential cross sections for two ranges of z: the red lines are for $|z| < 0.6$, as in the Belle measurement, the black lines are for $|z| \leq 1$ (full range). Panel (a) shows the distribution in proton-antiproton invariant mass ($M_{p\bar{p}} \equiv W_{\gamma\gamma}$). The $M_{p\bar{p}}$ distribution for the full z-range extends to much larger invariant masses while for the Belle z-range it falls steeply down. Similar as for the elementary cross section (Fig. 7), the hand-bag mechanism contributes significantly at $M_{p\bar{p}} > 3$ GeV. Simultaneously, the difference between the results with (solid lines) and without (dotted lines) hand-bag contribution appears more pronounced for the case when the angular phase space is narrowed. In the present calculations we integrate for $2m_p \leq W_{\gamma\gamma} < 4$ GeV. The transverse momentum distributions of protons and antiprotons shown in panel (b) are identical. Therefore we label them by p_t. For large p_t the distributions fall steeply. The limitation on the phase space ($|z| < 0.6$) has a significant impact for smaller values of p_t and has no

influence for $p_t > 1.4$ GeV. In the panel (c) we show distributions in rapidity of the proton or antiproton (which are identical). Here we see only a difference in the normalization, and not in the shape for the two different ranges of z. Finally, in the panel (d) we show the distribution in rapidity distance between proton and antiproton $y_{diff} = y_p - y_{\bar{p}}$. The larger the range of phase space the broader is the distribution in y_{diff}. There are three maxima when no extra cuts are imposed. The broad peak at $y_{diff} \approx 0$ corresponds to the region $|z| < 0.6$. It seems that observation of the broader y_{diff} distribution, in particular identification of the outer maxima, could be a good test of our model. As we see from Fig. 12 the cross section decreases quickly with $W_{\gamma\gamma} = M_{p\bar{p}}$ for $|z| < 0.6$, but stays large for $|z| \to 1$. Thus, extending the integration to $W_{\gamma\gamma} > 4$ GeV should not change the distributions of Fig. 14(b)–(d) for $|z| < 0.6$ but could have a sizeable influence on those for $|z| \leq 1$.

In Fig. 15 we show the two-dimensional distributions in $(y_p, y_{\bar{p}})$ again for two ranges of z (left panel relates to the Belle angle limitation and right panel is for full phase
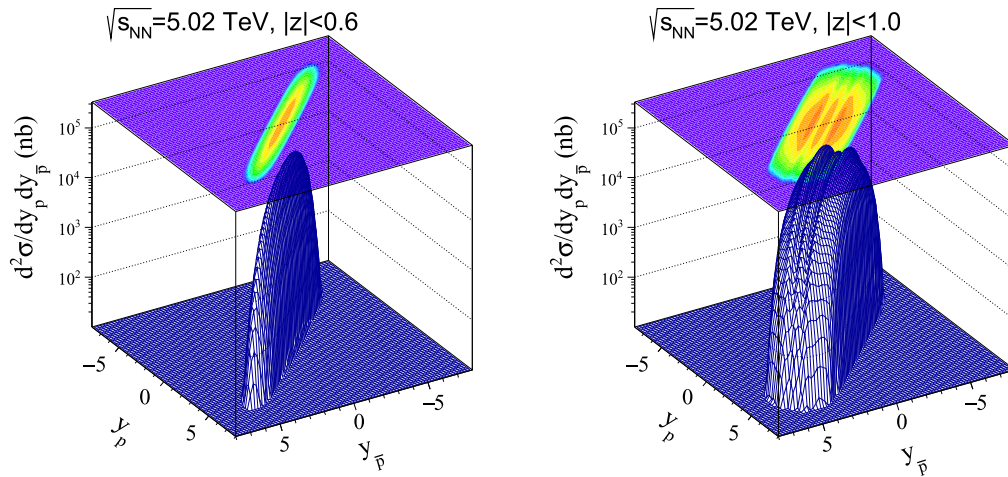
FIG. 15.   The two-dimensional distributions in proton and antiproton rapidities for the reaction (3.1) at $\sqrt{s_{NN}} = 5.02$ TeV for two different z-ranges of outgoing nucleons. The results include the hand-bag contribution. The results are integrated for $2m_p < W_{\gamma\gamma} < 4$ GeV.
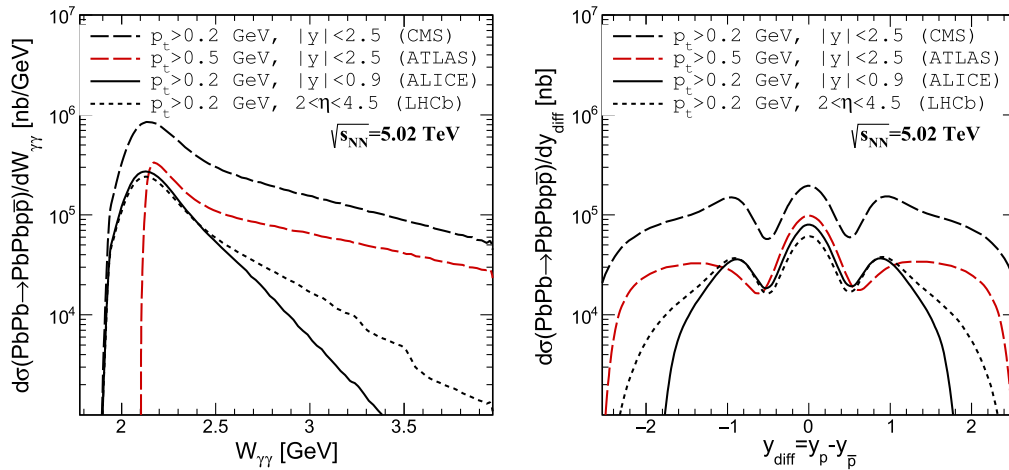

FIG. 16.   The differential nuclear cross sections as a function of $p\bar{p}$ invariant mass (the left panel) and $y_{\text{diff}} = y_p - y_{\bar{p}}$ (the right panel) for the $PbPb \to PbPbp\bar{p}$ reaction (3.1). The results for different experimental cuts are presented.

space). The cross section is concentrated along the diagonal $y_p \simeq y_{\bar{p}}$.

The ALICE Collaboration can measure $p\bar{p}$ in Pb-Pb collisions for $|y| < 0.9$; see [26] where the $J/\psi \to p\bar{p}$ decay was observed.[3] We predict 46 events for $|y| < 0.9$ and $p_t > 1$ GeV for our $\gamma\gamma \to p\bar{p}$ contribution, including three mechanisms, for ALICE integrated luminosity $L_{\text{int}} = 95$ μb^{-1} [26]. On the other hand the coherent J/ψ photoproduction [27] in the $p\bar{p}$ channel gives 583 events assuming approximately isotropic decay of $J/\psi \to p\bar{p}$. This strongly suggests dominance of the coherent photoproduction mechanism of J/ψ over the $\gamma\gamma$ contribution. With such a transverse momentum cut as for the ALICE

preliminary result a lot of the $\gamma\gamma \to p\bar{p}$ contribution is lost (with respect to the full phase space) but considerably less of coherent $J/\psi \to p\bar{p}$ contribution, where the maximum of the $p\bar{p}$ emission occurs at $p_t = \frac{m_{J/\psi}}{2} \approx 1.5$ GeV (sharp Jacobian peak associated with the fact that transverse momentum of the coherent J/ψ is very small). Generally, the range covered by the ATLAS and CMS detectors for $p\bar{p}$ pairs in UPC is somewhat larger, $|y| < 2.5$. The LHCb Collaboration can measure $p\bar{p}$ production in nuclear collisions for $2 < \eta < 4.5$ and $p_t > 0.2$ GeV.[4]

In Fig. 16 we present distributions in $W_{\gamma\gamma} \equiv M_{p\bar{p}}$ (the left panel) and $y_{\text{diff}} = y_p - y_{\bar{p}}$ (the right panel) imposing

---

[3]We thank E. L. Kryshen for some information on the recent ALICE measurement.

[4]We thank R. McNulty and T. Shears for some information on the recent LHCb measurement.

cuts on rapidities and transverse momenta of outgoing baryons. From the left panel, we can observe that the dependence on invariant mass of the $p\bar{p}$ pair is sensitive to the (pseudo)rapidity cut imposed. Note that due to the cut on $p_t > 0.5$ GeV the $W_{\gamma\gamma}$ distribution begins with a larger value of 2.1 GeV (compare also with Fig. 14(a)). The distribution in the difference of proton and antiproton rapidities is interesting. Again (comparing with Fig. 14(d), $|z| < 1.0$) the y_{diff}-distributions show three maxima. The experimental cuts imposed on p_t do not remove the external maxima predicted by our model. Such characteristic features can be checked by future experiments.

For completeness, we give the cross sections for the $PbPb \to PbPbp\bar{p}$ reaction for the $\gamma\gamma$ contribution for various experimental cuts on proton and antiproton (pseudo) rapidities and transverse momenta at $\sqrt{s_{NN}} = 5.02$ TeV. We find the cross section of 100 μb taking into account the ALICE cuts ($|y| < 0.9$, $p_t > 0.2$ GeV), 160 μb for the ATLAS cuts ($|y| < 2.5$, $p_t > 0.5$ GeV), 500 μb for the CMS cuts ($|y| < 2.5$, $p_t > 0.2$ GeV), and 104 μb for the LHCb cuts ($2 < \eta < 4.5$, $p_t > 0.2$ GeV).

VI. CONCLUSIONS

We have discussed in detail the production of proton-antiproton pairs in photon-photon collisions. Previous theoretical papers on the subject tried to pick up only one simple mechanism out of many in principle possible ones. In our work we have tried to incorporate the known mechanisms, such as proton exchange, s-channel resonance exchange, and the hand-bag contribution.

In our calculation of the nonresonant proton exchange we have included both Dirac- and Pauli-type couplings of the photon to the nucleon and form factors for the exchanged off-shell protons. We have found that the Pauli-type coupling is very important, enhances the cross section considerably, and cannot therefore be neglected.

We have shown that the Belle data [5] for low photon-photon energies can be nicely described by including in addition to the proton exchange the s-channel exchange of the $f_2(1950)$ resonance, which was observed to decay into the $\gamma\gamma$ and $p\bar{p}$ channels [24]. We include in the calculation also the s-channel $f_2(1270)$ meson exchange contribution. These two tensor mesons were also needed to describe the Belle data for the $\gamma\gamma \to \pi^+\pi^-$ and $\gamma\gamma \to \pi^0\pi^0$ processes [16,28]. Our simple model has a few parameters; see Table II. Adjusting the parameters of the vertex form factors for the proton exchange, of the tensor meson s-channel exchanges, and of the form factor (2.34) in the hand-bag contribution we have managed to describe both total cross section and differential angular distributions of the Belle Collaboration with significantly better agreement with the data than in all previous trials.

Having described the Belle data we have used the $\gamma\gamma \to p\bar{p}$ cross section to calculate the integrated cross section and differential distributions for production of $p\bar{p}$ pairs in ultraperipheral, ultrarelativistic, collisions (UPC) of heavy ions at $\sqrt{s_{NN}} = 5.02$ TeV. We have presented distributions in rapidity and transverse momentum of protons and antiprotons, invariant mass of the $p\bar{p}$ system as well as in the difference of rapidities for protons and antiprotons. We have presented results for the full angular range of $z = \cos\theta$ as well as for the Belle range $|z| < 0.6$. The integrated cross section for the full phase space is by a factor 5 larger than the one corresponding to the Belle angular coverage. The larger the range of phase space the broader is the distribution in y_{diff}, the rapidity difference between proton and antiproton.

We have also made predictions for $Pb - Pb$ collisions at $\sqrt{s_{NN}} = 5.02$ TeV and experimental cuts for the ALICE, ATLAS, CMS, and LHCb experiments. Corresponding total cross sections and differential distributions have been presented. The UPC of heavy ions may provide new information compared to the presently available data from e^+e^- collisions, in particular, if the structures of the y_{diff} distributions shown in Figs. 14 and 16 can be observed.

## APPENDIX A: HELICITY STATES FOR PROTONS AND ANTIPROTONS AND HELICITY AMPLITUDES

The general theory of helicity amplitudes for collisions of particles with spin was developed in [29]. To make our article self-contained and to fix the phases of our states we discuss in the following the construction of helicity states for protons and antiprotons as we found convenient for our purposes. These states are then used to determine the independent helicity amplitudes for the reaction $\gamma\gamma \to p\bar{p}$ (2.1).

We consider protons and antiprotons in a fixed reference frame; see Fig. 17. Let $\boldsymbol{p}$ be the 3-momentum of the proton and

$$\hat{\boldsymbol{p}} = \frac{\boldsymbol{p}}{|\boldsymbol{p}|} = \begin{pmatrix} \sin\theta\cos\phi \\ \sin\theta\sin\phi \\ \cos\theta \end{pmatrix},$$

$$0 \le \theta \le \pi, \qquad \le \phi < 2\pi. \tag{A1}$$

We use throughout our paper a boldface notation for 3-vectors, $\boldsymbol{p}$, $\boldsymbol{e}_z$, etc.
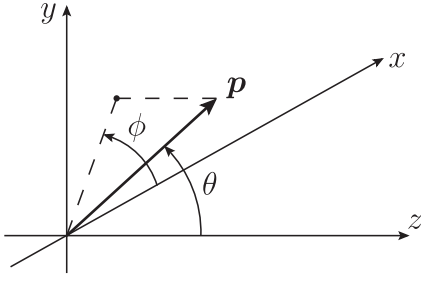
FIG. 17. Coordinate system and momentum vector $\boldsymbol{p}$.

For $\hat{\boldsymbol{p}} \cdot \boldsymbol{e}_z \neq -1$ ($\theta \neq \pi$) we define the spinors of definite helicity of type a as

$$u_s^{(h,a)}(p) = \sqrt{p^0 + m_p}\begin{pmatrix} \chi_s^{(a)}(\hat{\boldsymbol{p}}) \\ 2s\frac{|\boldsymbol{p}|}{p^0+m_p}\chi_s^{(a)}(\hat{\boldsymbol{p}}) \end{pmatrix},$$
$$s \in \{+1/2, -1/2\}, \tag{A2}$$

where

$$\chi_s^{(a)}(\hat{\boldsymbol{p}}) = \frac{1 + 2s(\boldsymbol{\sigma}\cdot\hat{\boldsymbol{p}})}{\sqrt{2(1+\hat{\boldsymbol{p}}\cdot\boldsymbol{e}_z)}}\chi_s^{(1)},$$
$$\chi_{1/2}^{(1)} = \begin{pmatrix} 1 \\ 0 \end{pmatrix}, \qquad \chi_{-1/2}^{(1)} = \begin{pmatrix} 0 \\ 1 \end{pmatrix}. \tag{A3}$$

This gives

$$\chi_{1/2}^{(a)}(\hat{\boldsymbol{p}}) = \frac{1}{\sqrt{2}}\begin{pmatrix} \sqrt{1+\hat{p}_z} \\ \frac{\hat{p}_x+i\hat{p}_y}{\sqrt{1+\hat{p}_z}} \end{pmatrix} = \begin{pmatrix} \cos\frac{\theta}{2} \\ \sin\frac{\theta}{2}e^{i\phi} \end{pmatrix},$$

$$\chi_{-1/2}^{(a)}(\hat{\boldsymbol{p}}) = \frac{1}{\sqrt{2}}\begin{pmatrix} -\frac{\hat{p}_x-i\hat{p}_y}{\sqrt{1+\hat{p}_z}} \\ \sqrt{1+\hat{p}_z} \end{pmatrix} = \begin{pmatrix} -\sin\frac{\theta}{2}e^{-i\phi} \\ \cos\frac{\theta}{2} \end{pmatrix}, \tag{A4}$$

$$\bar{u}_r^{(h,a)}(p)u_s^{(h,a)}(p) = 2m_p\delta_{rs}. \tag{A5}$$

Let us denote the usual spinors with spin in $\pm z$ direction as

$$u_r(p) = \sqrt{p^0 + m_p}\begin{pmatrix} \chi_r^{(1)} \\ \frac{\boldsymbol{\sigma}\cdot\boldsymbol{p}}{p^0+m_p}\chi_r^{(1)} \end{pmatrix},$$
$$r \in \{+1/2, -1/2\}; \tag{A6}$$

see for instance [30].

We get then

$$(\bar{u}_r(p)u_s^{(h,a)}(p)) = 2m_p(B_{rs}^{(a)}(\hat{\boldsymbol{p}})),$$
$$B^{(a)}(\hat{\boldsymbol{p}}) = (B_{rs}^{(a)}(\hat{\boldsymbol{p}}))$$
$$= \frac{1}{\sqrt{2}}\begin{pmatrix} \sqrt{1+\hat{p}_z} & -\frac{\hat{p}_x-i\hat{p}_y}{\sqrt{1+\hat{p}_z}} \\ \frac{\hat{p}_x+i\hat{p}_y}{\sqrt{1+\hat{p}_z}} & \sqrt{1+\hat{p}_z} \end{pmatrix}$$
$$= \begin{pmatrix} \cos\frac{\theta}{2} & -\sin\frac{\theta}{2}e^{-i\phi} \\ \sin\frac{\theta}{2}e^{i\phi} & \cos\frac{\theta}{2} \end{pmatrix}. \tag{A7}$$

Furthermore we define the creation operators for a proton in the helicity state s of type a by

$$a_{h,a}^\dagger(\boldsymbol{p}, s) = a_r^\dagger(\boldsymbol{p})B_{rs}^{(a)}(\hat{\boldsymbol{p}}), \tag{A8}$$

where $a_r^\dagger(\boldsymbol{p})$ are the usual creation operators corresponding to the spinors (A6). We have then

$$u_s^{(h,a)}(p)\bar{u}_s^{(h,a)}(p) = \not{p} + m_p,$$
$$a_{h,a}^\dagger(\boldsymbol{p}, s)\bar{u}_s^{(h,a)}(p) = a_r^\dagger(\boldsymbol{p})\bar{u}_r(p). \tag{A9}$$

For $\hat{\boldsymbol{p}} \cdot \boldsymbol{e}_z \neq 1$ ($\theta \neq 0$) we can define helicity spinors of type b as follows

$$u_s^{(h,b)}(p) = \sqrt{p^0 + m_p}\begin{pmatrix} \chi_s^{(b)}(\hat{\boldsymbol{p}}) \\ 2s\frac{|\boldsymbol{p}|}{p^0+m_p}\chi_s^{(b)}(\hat{\boldsymbol{p}}) \end{pmatrix},$$
$$\chi_s^{(b)}(\hat{\boldsymbol{p}}) = \frac{1 + 2s(\boldsymbol{\sigma}\cdot\hat{\boldsymbol{p}})}{\sqrt{2(1-\hat{\boldsymbol{p}}\cdot\boldsymbol{e}_z)}}\chi_{-s}^{(1)},$$
$$s \in \{+1/2, -1/2\}. \tag{A10}$$

This gives

$$\chi_{1/2}^{(b)}(\hat{\boldsymbol{p}}) = \frac{1}{\sqrt{2}}\begin{pmatrix} \frac{\hat{p}_x-i\hat{p}_y}{\sqrt{1-\hat{p}_z}} \\ \sqrt{1-\hat{p}_z} \end{pmatrix} = \begin{pmatrix} \cos\frac{\theta}{2}e^{-i\phi} \\ \sin\frac{\theta}{2} \end{pmatrix},$$

$$\chi_{-1/2}^{(b)}(\hat{\boldsymbol{p}}) = \frac{1}{\sqrt{2}}\begin{pmatrix} \sqrt{1-\hat{p}_z} \\ -\frac{\hat{p}_x+i\hat{p}_y}{\sqrt{1-\hat{p}_z}} \end{pmatrix} = \begin{pmatrix} \sin\frac{\theta}{2} \\ -\cos\frac{\theta}{2}e^{i\phi} \end{pmatrix}. \tag{A11}$$

Comparing with (A4) we find for $0 < \theta < \pi$

$$\chi_{1/2}^{(b)}(\hat{\boldsymbol{p}}) = e^{-i\phi}\chi_{1/2}^{(a)}(\hat{\boldsymbol{p}}),$$
$$\chi_{-1/2}^{(b)}(\hat{\boldsymbol{p}}) = -e^{i\phi}\chi_{-1/2}^{(a)}(\hat{\boldsymbol{p}}). \tag{A12}$$

With $u_r(p)$ from (A6) we find

$$(\bar{u}_r(p)u_s^{(h,b)}(p)) = 2m_p(B_{rs}^{(b)}(\hat{\boldsymbol{p}})),$$

$$B^{(b)}(\hat{\boldsymbol{p}}) = (B_{rs}^{(b)}(\hat{\boldsymbol{p}}))$$

$$= \frac{1}{\sqrt{2}}\begin{pmatrix} \frac{\hat{p}_x - i\hat{p}_y}{\sqrt{1-\hat{p}_z}} & \sqrt{1-\hat{p}_z} \\ \sqrt{1-\hat{p}_z} & -\frac{\hat{p}_x + i\hat{p}_y}{\sqrt{1-\hat{p}_z}} \end{pmatrix}$$

$$= \begin{pmatrix} \cos\frac{\theta}{2}e^{-i\phi} & \sin\frac{\theta}{2} \\ \sin\frac{\theta}{2} & -\cos\frac{\theta}{2}e^{i\phi} \end{pmatrix}. \tag{A13}$$

Defining creation operators analogous to (A8)

$$a_{h,b}^\dagger(\boldsymbol{p}, s) = a_r^\dagger(\boldsymbol{p})B_{rs}^{(b)}(\hat{\boldsymbol{p}}), \tag{A14}$$

we get

$$u_s^{(h,b)}(p)\bar{u}_s^{(h,b)}(p) = \slashed{p} + m_p,$$

$$a_{h,b}^\dagger(\boldsymbol{p}, s)\bar{u}_s^{(h,b)}(p) = a_r^\dagger(\boldsymbol{p})\bar{u}_r(p). \tag{A15}$$

Now we go to antiprotons. For this we use the charge-conjugation matrix

$$S(C) = i\gamma^2\gamma^0 = -i\gamma_2\gamma_0 = \begin{pmatrix} 0 & -\varepsilon \\ -\varepsilon & 0 \end{pmatrix},$$

$$\varepsilon = \begin{pmatrix} 0 & 1 \\ -1 & 0 \end{pmatrix}; \tag{A16}$$

see for instance chapter 4 of [30]. We have

$$S(C) = \bar{S}(C) = -S^{-1}(C) = -S(C)^\dagger = -S(C)^T,$$

$$S^{-1}(C)\gamma^\mu S(C) = -\gamma^{\mu T}. \tag{A17}$$

We define the antiproton spinors as

$$\bar{v}_r(p) = u_r^T(p)S(C)$$
$$= -\sqrt{p^0 + m_p}\left(-\chi_r^{(1)T}\varepsilon\frac{\boldsymbol{\sigma}\cdot\boldsymbol{p}}{p^0 + m_p}, \chi_r^{(1)T}\varepsilon\right), \tag{A18}$$

$$\bar{v}_s^{(h,a)}(p) = u_s^{T(h,a)}(p)S(C)$$
$$= -\sqrt{p^0 + m_p}\left(\chi_s^{(a)T}(\hat{\boldsymbol{p}})\varepsilon 2s\frac{|\boldsymbol{p}|}{p^0 + m_p}, \chi_s^{(a)T}(\hat{\boldsymbol{p}})\varepsilon\right), \tag{A19}$$

$$\bar{v}_s^{(h,b)}(p) = u_s^{T(h,b)}(p)S(C)$$
$$= -\sqrt{p^0 + m_p}\left(\chi_s^{(b)T}(\hat{\boldsymbol{p}})\varepsilon 2s\frac{|\boldsymbol{p}|}{p^0 + m_p}, \chi_s^{(b)T}(\hat{\boldsymbol{p}})\varepsilon\right); \tag{A20}$$

see (A6), (A2), and (A10).

The creation operators for antiprotons are in the standard basis

$$b_r^\dagger(\boldsymbol{p}) = U(C)a_r^\dagger(\boldsymbol{p})U^{-1}(C), \tag{A21}$$

where $U(C)$ is the charge-conjugation operator. Analogously we define the creation operators for antiprotons of definite helicity

$$b_{h,a}^\dagger(\boldsymbol{p}, s) = U(C)a_{h,a}^\dagger(\boldsymbol{p}, s)U^{-1}(C) = b_r^\dagger(\boldsymbol{p})B_{rs}^{(a)}(\hat{\boldsymbol{p}}), \tag{A22}$$

$$b_{h,b}^\dagger(\boldsymbol{p}, s) = U(C)a_{h,b}^\dagger(\boldsymbol{p}, s)U^{-1}(C) = b_r^\dagger(\boldsymbol{p})B_{rs}^{(b)}(\hat{\boldsymbol{p}}), \tag{A23}$$

where we used (A8) and (A14).

With this we get

$$v_s^{(h,a)}(p)\bar{v}_s^{(h,a)}(p) = \slashed{p} - m_p,$$

$$v_s^{(h,b)}(p)\bar{v}_s^{(h,b)}(p) = \slashed{p} - m_p, \tag{A24}$$

$$v_s^{(h,a)}(p)b_{h,a}^\dagger(\boldsymbol{p}, s) = v_r(p)b_r^\dagger(\boldsymbol{p}),$$

$$v_s^{(h,b)}(p)b_{h,b}^\dagger(\boldsymbol{p}, s) = v_r(p)b_r^\dagger(\boldsymbol{p}). \tag{A25}$$

Now we come to the reaction (2.1). We consider (2.1) in the c.m. system with the x-z plane giving the reaction plane; see Fig. 18. The usual kinematic variables are given by (2.5). Let $\boldsymbol{e}_x$, $\boldsymbol{e}_y$, $\boldsymbol{e}_z$ be the Cartesian unit vectors in the reference system of Fig. 18. Then $k_1^0 = k_2^0 = p_3^0 = p_4^0 = \frac{1}{2}\sqrt{s}$ and the momenta of the particles are

$$\boldsymbol{k_1} = -\boldsymbol{k_2} = |\boldsymbol{k_1}|\boldsymbol{e}_z,$$

$$\boldsymbol{p_3} = -\boldsymbol{p_4} = |\boldsymbol{p_3}|(\sin\theta\boldsymbol{e}_x + \cos\theta\boldsymbol{e}_z),$$

$$|\boldsymbol{k_1}| = \frac{1}{2}\sqrt{s},$$

$$|\boldsymbol{p_3}| = \frac{1}{2}\sqrt{s - 4m_p^2}. \tag{A26}$$

As polarization vectors for the incoming photons of definite helicity we choose
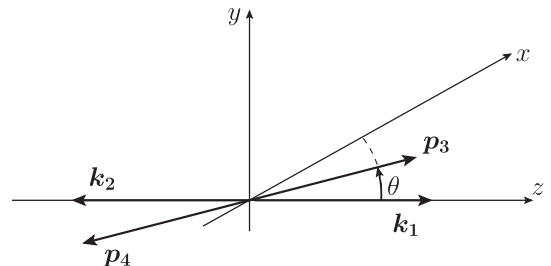

FIG. 18. The reaction $\gamma\gamma \to p\bar{p}$ in the c.m. system.

TABLE III.   Transformation properties of creation operators for protons, antiprotons, and photons under the transformations (A31) and (A32).

$A^\dagger$	$U_2(\pi)U(P)A^\dagger U^{-1}(P)U_2^{-1}(\pi)$	$U_2(\pi)U(C)A^\dagger U^{-1}(C)U_2^{-1}(\pi)$
$a_s^\dagger(\boldsymbol{p_3})$	$-a_r^\dagger(\boldsymbol{p_3})\varepsilon_{rs}$	$-b_r^\dagger(\boldsymbol{p_4})\varepsilon_{rs}$
$b_s^\dagger(\boldsymbol{p_4})$	$b_r^\dagger(\boldsymbol{p_4})\varepsilon_{rs}$	$-a_r^\dagger(\boldsymbol{p_3})\varepsilon_{rs}$
$a_{h,a}^\dagger(\boldsymbol{p_3},s)$	$-a_{h,a}^\dagger(\boldsymbol{p_3},r)\varepsilon_{rs}$	$b_{h,b}^\dagger(\boldsymbol{p_4},r)(\sigma_3)_{rs}$
$b_{h,b}^\dagger(\boldsymbol{p_4},s)$	$-b_{h,b}^\dagger(\boldsymbol{p_4},r)\varepsilon_{rs}$	$-a_{h,a}^\dagger(\boldsymbol{p_3},r)(\sigma_3)_{rs}$
$a^\dagger(\boldsymbol{k_1},m)$	$-a^\dagger(\boldsymbol{k_1},-m)$	$-a^\dagger(\boldsymbol{k_2},m)$
$a^\dagger(\boldsymbol{k_2},m)$	$-a^\dagger(\boldsymbol{k_2},-m)$	$-a^\dagger(\boldsymbol{k_1},m)$

$$\boldsymbol{\epsilon}_1^{(\pm)} = \mp\frac{1}{\sqrt{2}}(\boldsymbol{e}_x \pm i\boldsymbol{e}_y),$$

$$\boldsymbol{\epsilon}_2^{(\pm)} = \mp\frac{1}{\sqrt{2}}(-\boldsymbol{e}_x \pm i\boldsymbol{e}_y). \tag{A27}$$

The corresponding photon creation operators are

$$a^\dagger(\boldsymbol{k}_j,m) = \boldsymbol{\epsilon}_j^{(m)}\boldsymbol{a}^\dagger(\boldsymbol{k}_j),$$

$$j = 1,2, \quad m = \pm 1. \tag{A28}$$

For the proton we choose the helicity basis a, for the antiproton the basis b. From (A8) and (A23) we have for the corresponding creation operators

$$a_{h,a}^\dagger(\boldsymbol{p}_3,s) = a_r^\dagger(\boldsymbol{p}_3)B_{rs}^{(a)}(\hat{\boldsymbol{p}}_3), \tag{A29}$$

$$b_{h,b}^\dagger(\boldsymbol{p}_4,s) = b_r^\dagger(\boldsymbol{p}_4)B_{rs}^{(b)}(\hat{\boldsymbol{p}}_4). \tag{A30}$$

Note that in calculating $B_{rs}^{(a)}(\hat{\boldsymbol{p}}_3)$ from (A7) we have to make the replacements $\theta \to \theta$, $\phi \to 0$. Calculating $B_{rs}^{(b)}(\hat{\boldsymbol{p}}_4)$ from (A13) we have to make the replacements $\theta \to \pi - \theta$, $\phi \to \pi$.

The symmetries of the reaction (2.1) are the following. The parity (P) transformation followed by a rotation by π around the positive y-axis:

$$U_2(\pi)U(P). \tag{A31}$$

The charge-conjugation (C) transformation followed by a rotation by π around the positive y-axis:

$$U_2(\pi)U(C). \tag{A32}$$

From the transformation laws of the standard creation operators (see, e.g., [30]) and from the relations [see (A7), (A13)]

$$\varepsilon^T B^{(a)}(\hat{\boldsymbol{p}}_3)\varepsilon = B^{(a)}(\hat{\boldsymbol{p}}_3),$$

$$\varepsilon^T B^{(b)}(\hat{\boldsymbol{p}}_4)\varepsilon = -B^{(b)}(\hat{\boldsymbol{p}}_4), \tag{A33}$$

$$\varepsilon B^{(a)}(\hat{\boldsymbol{p}}_3) = -B^{(b)}(\hat{\boldsymbol{p}}_4)\sigma_3,$$

$$\varepsilon B^{(b)}(\hat{\boldsymbol{p}}_4) = B^{(a)}(\hat{\boldsymbol{p}}_3)\sigma_3, \tag{A34}$$

we get the transformation laws for the helicity creation operators shown in Table III.

We define now the helicity states for the reaction (2.1) using (A28), (A29), and (A30) as

$$|\gamma(\boldsymbol{k}_1,m_1),\gamma(\boldsymbol{k}_2,m_2)\rangle = a^\dagger(\boldsymbol{k}_1,m_1)a^\dagger(\boldsymbol{k}_2,m_2)|0\rangle,$$

$$m_1, m_2 \in \{+1,-1\},$$

$$|p(\boldsymbol{p}_3,s_3),\bar{p}(\boldsymbol{p}_4,s_4)\rangle = a_{h,a}^\dagger(\boldsymbol{p}_3,s_3)b_{h,b}^\dagger(\boldsymbol{p}_4,s_4)|0\rangle,$$

$$s_3, s_4 \in \{+1/2,-1/2\}. \tag{A35}$$

The transformation laws of these states are shown in Table IV.

Finally we come to the helicity amplitudes for the reaction (2.1)

$$\langle p(\boldsymbol{p}_3,s_3),\bar{p}(\boldsymbol{p}_4,s_4)|\mathcal{T}|\gamma(\boldsymbol{k}_1,m_1),\gamma(\boldsymbol{k}_2,m_2)\rangle$$

$$\equiv \langle 2s_3, 2s_4|\mathcal{T}|m_1,m_2\rangle,$$

$$2s_3, 2s_4, m_1, m_2 \in \{+1,-1\}, \tag{A36}$$

where we use the convenient short-hand notation of (2.8). There are 16 helicity amplitudes. The symmetry $U_2(\pi)U(P)$ (A31) gives the relation, using Table IV,

$$\langle 2s_3, 2s_4|\mathcal{T}|m_1,m_2\rangle = \langle 2r_3, 2r_4|\mathcal{T}|-m_1,-m_2\rangle\varepsilon_{r_3s_3}\varepsilon_{r_4s_4}. \tag{A37}$$

From the symmetry of $U_2(\pi)U(C)$ (A32) we get

TABLE IV.   Transformation laws of the states (A35) under the transformations (A31) and (A32).

$|\rangle$	$U_2(\pi)U(P)|\rangle$	$U_2(\pi)U(C)|\rangle$
$|p(\boldsymbol{p}_3,s_3),\bar{p}(\boldsymbol{p}_4,s_4)\rangle$	$|p(\boldsymbol{p}_3,r_3),\bar{p}(\boldsymbol{p}_4,r_4)\rangle\varepsilon_{r_3s_3}\varepsilon_{r_4s_4}$	$|p(\boldsymbol{p}_3,r_3),\bar{p}(\boldsymbol{p}_4,r_4)\rangle(\sigma_3)_{r_3s_4}(\sigma_3)_{r_4s_3}$
$|\gamma(\boldsymbol{k}_1,m_1),\gamma(\boldsymbol{k}_2,m_2)\rangle$	$|\gamma(\boldsymbol{k}_1,-m_1),\gamma(\boldsymbol{k}_2,-m_2)\rangle$	$|\gamma(\boldsymbol{k}_1,m_2),\gamma(\boldsymbol{k}_2,m_1)\rangle$

TABLE V. Helicity amplitudes for $\gamma\gamma \to p\bar{p}$ (2.1) and their symmetry relations.

	$U_2(\pi)U(P)$	$U_2(\pi)U(C)$	
$\langle++|\mathcal{T}|++\rangle$	$\langle--|\mathcal{T}|--\rangle$	$\langle++|\mathcal{T}|++\rangle$	ψ_1
$\langle+-|\mathcal{T}|++\rangle$	$-\langle-+|\mathcal{T}|--\rangle$	$-\langle-+|\mathcal{T}|++\rangle$	ψ_6
$\langle-+|\mathcal{T}|++\rangle$	$-\langle+-|\mathcal{T}|--\rangle$	$-\langle+-|\mathcal{T}|++\rangle$	$-\psi_6$
$\langle--|\mathcal{T}|++\rangle$	$\langle++|\mathcal{T}|--\rangle$	$\langle--|\mathcal{T}|++\rangle$	ψ_2
$\langle++|\mathcal{T}|+-\rangle$	$\langle--|\mathcal{T}|-+\rangle$	$\langle++|\mathcal{T}|-+\rangle$	ψ_5
$\langle+-|\mathcal{T}|+-\rangle$	$-\langle-+|\mathcal{T}|-+\rangle$	$-\langle-+|\mathcal{T}|-+\rangle$	ψ_3
$\langle-+|\mathcal{T}|+-\rangle$	$-\langle+-|\mathcal{T}|-+\rangle$	$-\langle+-|\mathcal{T}|-+\rangle$	$-\psi_4$
$\langle--|\mathcal{T}|+-\rangle$	$\langle++|\mathcal{T}|-+\rangle$	$\langle--|\mathcal{T}|-+\rangle$	ψ_5
$\langle++|\mathcal{T}|-+\rangle$	$\langle--|\mathcal{T}|+-\rangle$	$\langle++|\mathcal{T}|+-\rangle$	ψ_5
$\langle+-|\mathcal{T}|-+\rangle$	$-\langle-+|\mathcal{T}|+-\rangle$	$-\langle-+|\mathcal{T}|+-\rangle$	ψ_4
$\langle-+|\mathcal{T}|-+\rangle$	$-\langle+-|\mathcal{T}|+-\rangle$	$-\langle+-|\mathcal{T}|+-\rangle$	$-\psi_3$
$\langle--|\mathcal{T}|-+\rangle$	$\langle++|\mathcal{T}|+-\rangle$	$\langle--|\mathcal{T}|+-\rangle$	ψ_5
$\langle++|\mathcal{T}|--\rangle$	$\langle--|\mathcal{T}|++\rangle$	$\langle++|\mathcal{T}|--\rangle$	ψ_2
$\langle+-|\mathcal{T}|--\rangle$	$-\langle-+|\mathcal{T}|++\rangle$	$-\langle-+|\mathcal{T}|--\rangle$	ψ_6
$\langle-+|\mathcal{T}|--\rangle$	$-\langle+-|\mathcal{T}|++\rangle$	$-\langle+-|\mathcal{T}|--\rangle$	$-\psi_6$
$\langle--|\mathcal{T}|--\rangle$	$\langle++|\mathcal{T}|++\rangle$	$\langle--|\mathcal{T}|--\rangle$	ψ_1

$$\langle 2s_3, 2s_4 |\mathcal{T}| m_1, m_2 \rangle = \langle 2r_3, 2r_4 |\mathcal{T}| m_2, m_1 \rangle (\sigma_3)_{r_3 s_4} (\sigma_3)_{r_4 s_3}.$$
(A38)

The relations (A37) and (A38) are written explicitly for the helicity amplitudes in Table V. From this we find that there are only 6 independent helicity amplitudes for (2.1) which we choose as follows:

$$\psi_1(s, t) = \langle ++ |\mathcal{T}| ++ \rangle,$$
$$\psi_2(s, t) = \langle ++ |\mathcal{T}| -- \rangle,$$
$$\psi_3(s, t) = \langle +- |\mathcal{T}| +- \rangle,$$
$$\psi_4(s, t) = \langle +- |\mathcal{T}| -+ \rangle,$$
$$\psi_5(s, t) = \langle ++ |\mathcal{T}| +- \rangle,$$
$$\psi_6(s, t) = \langle +- |\mathcal{T}| ++ \rangle.$$
(A39)

With this we have obtained a complete overview of the general constraints of the helicity amplitudes of $\gamma\gamma \to p\bar{p}$ following from rotational, parity, and charge-conjugation invariance of strong and electromagnetic interactions.

Finally we note that the same analysis applies to any reaction

$$\gamma + \gamma \to B + \bar{B},$$
(A40)

where B stands for a spin $1/2$ baryon. We only have to replace in all our formulas m_p by m_B. Interesting examples may be $B = \Lambda, \Sigma^+, \Lambda_c^+$.[5] The polarization of these baryons can be obtained from their decay distributions.

---

[5]The Λ baryon has a magnetic moment $\mu_\Lambda = -0.613 \pm 0.004\mu_N$ [24]. Thus, the reaction $\gamma\gamma \to \Lambda\bar{\Lambda}$ can proceed through the analogue of the diagrams of Fig. 1(a) and 1(b).

TABLE VI. The l and S values leading to $p\bar{p}$ states with $J = 2$.

l	S	J^{PC}
2	0	2^{-+}
1	1	2^{++}
2	1	2^{--}
3	1	2^{++}

APPENDIX B: THE lS COUPLING SCHEME AND HELICITY AMPLITUDES FOR THE REACTION $\gamma\gamma \to f_2 \to p\bar{p}$

In this Appendix we discuss the relation of lS couplings to the helicity amplitudes for the reaction $\gamma\gamma \to f_2 \to p\bar{p}$. Here l stands for the orbital angular momentum and S for the total spin of the $p\bar{p}$ system.

Let us see in how many ways one can construct a $p\bar{p}$ state with $J^{PC} = 2^{++}$. The partial-wave analysis (which is perfectly relativistic) says that we can combine the spins of p and $\bar{p}$ to give the total spin $S = 0, 1$. Now we must combine this with the orbital angular momentum l to the total angular momentum $J = 2$. This gives the four possibilities listed in Table VI. In general we have the parity of $p\bar{p}$ state $P = (-1)^{l+1}$ (p and $\bar{p}$ have opposite intrinsic parity) and charge-conjugation $C = (-1)^{l+S}$. There are, thus, two possible (l, S) couplings for $f_2(2^{++}) \to p\bar{p}$: $(1,1)$ and $(3,1)$.

We shall now analyze the lS content of the $f_2 p\bar{p}$ couplings (2.19) and (2.20).

Let $u_r(p), v_r(p)$ be the usual Dirac spinors with spin in $\pm z$ direction for $r = \pm 1/2$; see (A6) and (A18). For these we find in the c.m. system of reaction (2.1) the matrix elements of the vertex functions $\Gamma_{\kappa\lambda}^{(f_2 p\bar{p})(j)}$ ($j = 1, 2$) [see (2.21), (2.22)] with $P^{(2)\kappa\lambda,\kappa'\lambda'}$ the spin 2 projector [the term in square brackets in (2.24)] as follows. For $j = 1$ we get

$$P^{(2)\kappa\lambda,\kappa'\lambda'}(p_3 + p_4)\bar{u}_{r_3}(p_3)\Gamma_{\kappa'\lambda'}^{(f_2 p\bar{p})(j)}(p_3, p_4)v_{r_4}(p_4) = 0$$

unless $\kappa = k, \lambda = l, \quad k, l \in \{1, 2, 3\},$
(B1)

$$P^{(2)kl,\kappa'\lambda'}(p_3 + p_4)\bar{u}_{r_3}(p_3)\Gamma_{\kappa'\lambda'}^{(f_2 p\bar{p})(1)}(p_3, p_4)v_{r_4}(p_4)$$

$$= -\frac{4g_{f_2 pp}^{(1)}}{M_0}F^{(f_2 p\bar{p})(1)}[(p_3 + p_4)^2]$$

$$\times \chi_{r_3}^\dagger \left\{ -p_3^0 \left[\frac{1}{2}p_3^k\sigma^l + \frac{1}{2}p_3^l\sigma^k - \frac{1}{3}\delta^{kl}(\boldsymbol{p_3}\cdot\boldsymbol{\sigma}) \right] \right.$$

$$\left. + \left[\frac{1}{2}p_3^k p_3^l + \frac{1}{2}p_3^l p_3^k - \frac{1}{3}\delta^{kl}|\boldsymbol{p_3}|^2 \right] \frac{1}{p_3^0 + m_p}(\boldsymbol{p_3}\cdot\boldsymbol{\sigma}) \right\} \varepsilon\chi_{r_4}^*.$$
(B2)

Here and in the following we set $\chi_r \equiv \chi_r^{(1)}$; see (A6) and (A18). For $j = 2$ we get

$$P^{(2)\kappa\lambda,\kappa'\lambda'}(p_3+p_4)\bar{u}_{r_3}(p_3)\Gamma^{(f_2 p\bar{p})(2)}_{\kappa'\lambda'}(p_3,p_4)v_{r_4}(p_4) = 0 \qquad \text{for } \kappa=0, \ \lambda \text{ arbitrary} \quad \text{and} \quad \kappa \text{ arbitrary}, \ \lambda=0; \quad \text{(B3)}$$

$$P^{(2)kl,\kappa'\lambda'}(p_3+p_4)\bar{u}_{r_3}(p_3)\Gamma^{(f_2 p\bar{p})(2)}_{\kappa'\lambda'}(p_3,p_4)v_{r_4}(p_4) = -\frac{8g^{(2)}_{f_2 pp}}{M_0^2}F^{(f_2 p\bar{p})(2)}[(p_3+p_4)^2]\left[p_3^k p_3^l - \frac{1}{3}\delta^{kl}|\boldsymbol{p_3}|^2\right]\boldsymbol{p_3}\cdot\chi^{\dagger}_{r_3}\boldsymbol{\sigma}\varepsilon\chi^*_{r_4}.$$

(B4)

The *l-S* amplitudes are as follows. For $l=1$, $S=1$ we have

$$\mathcal{A}^{kl}_{(1,1)} = \chi^{\dagger}_{r_3}\left[\frac{1}{2}p_3^k\sigma^l + \frac{1}{2}p_3^l\sigma^k - \frac{1}{3}\delta^{kl}(\boldsymbol{p_3}\cdot\boldsymbol{\sigma})\right]\varepsilon\chi^*_{r_4}. \tag{B5}$$

The traceless symmetric ($l=3$) tensor is

$$T^{klm}_3 = p_3^k p_3^l p_3^m - \frac{1}{5}|\boldsymbol{p_3}|^2(\delta^{kl}p_3^m + \delta^{km}p_3^l + \delta^{lm}p_3^k). \tag{B6}$$

This gives, for instance, with θ as defined in Fig. 18 and P_3 the Legendre polynomial

$$T^{klm}_3 e_z^k e_z^l e_z^m = |\boldsymbol{p_3}|^2\frac{2}{5}\left(\frac{5}{2}\cos^3\theta - \frac{3}{2}\cos\theta\right) = |\boldsymbol{p_3}|^2\frac{2}{5}P_3(\cos\theta). \tag{B7}$$

The $l=3$, $S=1$ the amplitude is

$$T^{klm}_3\chi^{\dagger}_{r_3}\sigma^m\varepsilon\chi^*_{r_4} = \mathcal{A}^{kl}_{(3,1)} = \left[p_3^k p_3^l - \frac{1}{3}\delta^{kl}|\boldsymbol{p_3}|^2\right]\chi^{\dagger}_{r_3}(\boldsymbol{p_3}\cdot\boldsymbol{\sigma})\varepsilon\chi^*_{r_4} - \frac{2}{5}|\boldsymbol{p_3}|^2\chi^{\dagger}_{r_3}\left[\frac{1}{2}p_3^k\sigma^l + \frac{1}{2}p_3^l\sigma^k - \frac{1}{3}\delta^{kl}(\boldsymbol{p_3}\cdot\boldsymbol{\sigma})\right]\varepsilon\chi^*_{r_4}. \quad \text{(B8)}$$

From (B2), (B4), (B5), and (B8) we get the $l-S$ decomposition of our couplings $j=1$ and 2 as follows:

$$P^{(2)kl,\kappa'\lambda'}(p_3+p_4)\bar{u}_{r_3}(p_3)\Gamma^{(f_2 p\bar{p})(1)}_{\kappa'\lambda'}(p_3,p_4)v_{r_4}(p_4) = -\frac{4g^{(1)}_{f_2 pp}}{M_0}F^{(f_2 p\bar{p})(1)}[(p_3+p_4)^2]$$
$$\times\left\{-\left(\frac{3}{5}p_3^0 + \frac{2}{5}m_p\right)\mathcal{A}^{kl}_{(1,1)} + \frac{1}{p_3^0+m_p}\mathcal{A}^{kl}_{(3,1)}\right\}, \tag{B9}$$

$$P^{(2)kl,\kappa'\lambda'}(p_3+p_4)\bar{u}_{r_3}(p_3)\Gamma^{(f_2 p\bar{p})(2)}_{\kappa'\lambda'}(p_3,p_4)v_{r_4}(p_4) = -\frac{8g^{(2)}_{f_2 pp}}{M_0^2}F^{(f_2 p\bar{p})(2)}[(p_3+p_4)^2]\times\left\{\frac{2}{5}((p_3^0)^2 - m_p^2)\mathcal{A}^{kl}_{(1,1)} + \mathcal{A}^{kl}_{(3,1)}\right\}.$$

(B10)

Note that—for χ_{r_3} and χ_{r_4} not depending on θ—$\mathcal{A}^{kl}_{(1,1)}$ clearly has only $l=1$ and $\mathcal{A}^{kl}_{(3,1)}$ clearly has only $l=3$; see (B5) and (B8), respectively.

But now we can go to the helicity amplitudes. All we have to do is to replace the two-component spinors as follows

$$\chi_{r_3} \to \chi^{(a)}_{s_3}(\hat{\boldsymbol{p_3}}) \text{ from (A4) with the replacements } \theta \to \theta, \ \phi \to 0,$$
$$\chi_{r_4} \to \chi^{(b)}_{s_4}(-\hat{\boldsymbol{p_3}}) \text{ from (A11) with the replacements } \theta \to \pi-\theta, \ \phi \to \pi. \tag{B11}$$

Note that these spinors depend on θ.
We get

$$(\chi^{(a)\dagger}_{s_3}\varepsilon\chi^{(b)*}_{s_4}) = \begin{pmatrix} 1 & 0 \\ 0 & -1 \end{pmatrix} = (\sigma^3_{s_3 s_4}), \qquad (\chi^{(a)\dagger}_{s_3}\sigma^1\varepsilon\chi^{(b)*}_{s_4}) = \begin{pmatrix} \sin\theta & -\cos\theta \\ \cos\theta & \sin\theta \end{pmatrix}, \qquad (\chi^{(a)\dagger}_{s_3}\sigma^2\varepsilon\chi^{(b)*}_{s_4}) = \begin{pmatrix} 0 & i \\ i & 0 \end{pmatrix},$$

$$(\chi^{(a)\dagger}_{s_3}\sigma^3\varepsilon\chi^{(b)*}_{s_4}) = \begin{pmatrix} \cos\theta & \sin\theta \\ -\sin\theta & \cos\theta \end{pmatrix}, \qquad (\chi^{(a)\dagger}_{s_3}\hat{\boldsymbol{p_3}}\cdot\boldsymbol{\sigma}\varepsilon\chi^{(b)*}_{s_4}) = \delta_{s_3 s_4}, \qquad \hat{\boldsymbol{p_3}} = \boldsymbol{p_3}/|\boldsymbol{p_3}|. \tag{B12}$$

Inserting these expressions in (B2) and (B4) we see that the $\boldsymbol{p_3}$ dependence, that is, the θ dependence of the amplitudes will in general be changed. Take, for instance, (B4) which is a combination of $l = 3$ plus $l = 1$; see (B5) and (B8). With the replacements (B11) we get from (B12)

$$\left[p_3^k p_3^l - \frac{1}{3}\delta^{kl}|\boldsymbol{p_3}|^2 \right] \chi_{s_3}^{(a)\dagger} \boldsymbol{p_3} \cdot \boldsymbol{\sigma}\varepsilon\chi_{s_4}^{(b)*}$$
$$= \left[p_3^k p_3^l - \frac{1}{3}\delta^{kl}|\boldsymbol{p_3}|^2 \right] |\boldsymbol{p_3}|\delta_{s_3 s_4}. \qquad \text{(B13)}$$

From $l = 3$ plus $l = 1$ we go, effectively, to $l = 2$.

The replacements (B11) lead from (B2) and (B4), using the expression for the diagram for $\gamma\gamma \to f_2 \to p\bar{p}$ [see Fig. 1(c)], to the helicity amplitudes (2.25) and (2.26).

APPENDIX C: PHASE CONVENTIONS

For the hand-bag contribution, Sec. II C, we must take into account different phase conventions used in [10] relative to ours, as explained in Appendix A. In [10] the orientation of the particle momenta corresponds to a rotation by $\frac{\pi}{2} - \theta$ relative to the momenta in Fig. 18. Considering this we find that their spinors for proton and antiproton correspond to our $u_{s_3}^{(h,a)}(p_3)$ and $-2s_4 v_{s_4}^{(h,b)}(p_4)$, respectively. The phase conventions for the photons are not stated explicitly in [10]. From a comparison[6] of the calculations (22) and (23) of [10] with the corresponding ones with our conventions we conclude that the $|\gamma(k_1, \pm), \gamma(k_2, \mp)\rangle$ states of [10] have an extra minus sign compared to ours. Taking everything together we obtain (2.33) for the amplitudes.

---

[6]We thank M. Diehl for correspondence on this point.

[1] M. Artuso *et al.* (CLEO Collaboration), Measurement of the cross section for $\gamma\gamma \to p\bar{p}$, Phys. Rev. D **50**, 5484 (1994).

[2] H. Hamasaki *et al.* (VENUS Collaboration), Measurement of the proton-antiproton pair production from two-photon collisions at TRISTAN, Phys. Lett. B **407**, 185 (1997).

[3] G. Abbiendi *et al.* (OPAL Collaboration), Measurement of the cross-section for the process $\gamma\gamma \to p\bar{p}$ at $\sqrt{s_{ee}} =$ 183–189 GeV at LEP, Eur. Phys. J. C **28**, 45 (2003).

[4] P. Achard *et al.* (L3 Collaboration), Proton-antiproton pair production in two-photon collisions at LEP, Phys. Lett. B **571**, 11 (2003).

[5] C. C. Kuo *et al.* (Belle Collaboration), Measurement of $\gamma\gamma \to p\bar{p}$ production at Belle, Phys. Lett. B **621**, 41 (2005).

[6] G. R. Farrar, E. Maina, and F. Neri, QCD predictions for $\gamma\gamma$ annihilation to baryons, Nucl. Phys. **B259**, 702 (1985); Erratum, Nucl. Phys. **B263**, 746 (1986).

[7] G. R. Farrar, H. Zhang, A. A. Ogloblin, and I. R. Zhitnitsky, Baryon wave functions and cross-sections for photon annihilation to baryon pairs, Nucl. Phys. **B311**, 585 (1989).

[8] V. L. Chernyak and I. R. Zhitnitsky, Nucleon wave function and nucleon form factors in QCD, Nucl. Phys. **B246**, 52 (1984).

[9] C. F. Berger and W. Schweiger, Hard exclusive baryon-antibaryon production in two-photon collisions, Eur. Phys. J. C **28**, 249 (2003).

[10] M. Diehl, P. Kroll, and C. Vogt, Two-photon annihilation into baryon anti-baryon pairs, Eur. Phys. J. C **26**, 567 (2003).

[11] K. Odagiri, Hadron pair photoproduction within the Veneziano model, Nucl. Phys. **A748**, 168 (2005).

[12] A. I. Ahmadov, A study of the process $e^+ + e^- \to e^+ + e^- + p + \bar{p}$ by the two-photon mechanism $\gamma\gamma \to p\bar{p}$ at high energies, Int. J. Mod. Phys. A **32**, 1750104 (2017).

[13] C. Ewerz, M. Maniatis, and O. Nachtmann, A model for soft high-energy scattering: Tensor Pomeron and vector Odderon, Ann. Phys. (Amsterdam) **342**, 31 (2014).

[14] M. Poppe, Exclusive hadron production in two photon reactions, Int. J. Mod. Phys. A **01**, 545 (1986).

[15] A. Szczurek and J. Speth, Perturbative QCD versus pion exchange and hadronic FSI effects in the $\gamma\gamma \to \pi^+\pi^-$ reaction, Nucl. Phys. **A728**, 182 (2003).

[16] M. Kłusek-Gawenda and A. Szczurek, $\pi^+\pi^-$ and $\pi^0\pi^0$ pair production in photon-photon scattering in ultraperipheral ultrarelativistic heavy ion collisions, Phys. Rev. C **87**, 054908 (2013).

[17] P. Lebiedowicz, O. Nachtmann, and A. Szczurek, ρ^0 and Drell-Söding contributions to central exclusive production of $\pi^+\pi^-$ pairs in proton-proton collisions at high energies, Phys. Rev. D **91**, 074023 (2015).

[18] P. Lebiedowicz, O. Nachtmann, and A. Szczurek, Central exclusive diffractive production of the $\pi^+\pi^-$ continuum, scalar, and tensor resonances in pp and $p\bar{p}$ scattering within the tensor Pomeron approach, Phys. Rev. D **93**, 054015 (2016).

[19] H. W. Huang, P. Kroll, and T. Morii, Perturbative and non-perturbative QCD corrections to wide-angle Compton scattering, Eur. Phys. J. C **23**, 301 (2002); Erratum, Eur. Phys. J. C **31**, 279 (2003).

[20] M. Kłusek-Gawenda and A. Szczurek, Exclusive muon-pair productions in ultrarelativistic heavy-ion collisions: Realistic nucleus charge form factor and differential distributions, Phys. Rev. C **82**, 014904 (2010).

[21] M. Kłusek-Gawenda, P. Lebiedowicz, and A. Szczurek, Light-by-light scattering in ultraperipheral Pb-Pb collisions at energies available at the CERN Large Hadron Collider, Phys. Rev. C **93**, 044907 (2016).

[22] M. Ablikim *et al.* (BES Collaboration), Measurement of $\psi(2S)$ Radiative Decays, Phys. Rev. Lett. **99**, 011802 (2007).

[23] J. P. Alexander *et al.* (CLEO Collaboration), Study of $\psi(2S)$ decays to $\gamma p\bar{p}$, $\pi^0 p\bar{p}$ and $\eta p\bar{p}$ and search for $p\bar{p}$ threshold enhancements, Phys. Rev. D **82**, 092002 (2010).

[24] C. Patrignani *et al.* (Particle Data Group), Review of particle physics, Chin. Phys. C **40**, 100001 (2016).

[25] P. Lebiedowicz and A. Szczurek, The role of meson exchanges in light-by-light scattering, Phys. Lett. B **772**, 330 (2017).

[26] E. L. Kryshen (ALICE Collaboration), Photoproduction of heavy vector mesons in ultra-peripheral Pb-Pb collisions, Nucl. Phys. **A967**, 273 (2017).

[27] M. Kłusek-Gawenda and A. Szczurek, Photoproduction of J/ψ mesons in peripheral and semicentral heavy ion collisions, Phys. Rev. C **93**, 044912 (2016).

[28] S. Uehara *et al.* (Belle Collaboration), High-statistics study of neutral-pion pair production in two-photon collisions, Phys. Rev. D **79**, 052009 (2009).

[29] M. Jacob and G. C. Wick, On the general theory of collisions for particles with spin, Ann. Phys. (N.Y.) **7**, 404 (1959); **281**, 774 (2000).

[30] O. Nachtmann, *Elementary Particle Physics: Concepts and Phenomena* (Springer-Verlag, Berlin, Heidelberg, 1990).